Egypt. J. Chem. **Vol. 68,** SI: Z. M. Nofal, pp. 339- 364 (2025)

Egyptian Journal of Chemistry

http://ejchem.journals.ekb.eg/

Hydrothermal Synthesis of Zeolite T from Bentonite Clay: Catalytic Applications and Molecular Docking Analysis

H. Taib[1],L. Lefrada[1] , D. Belfennache[*2], M. Y. Belghit[3], M. Benbouzid[1], S. YILMAZ[4], R.Yekhlef[2], M. Boukraa[2], Mohamed A.Ali[*5]

[1]*Analytical Sciences Laboratory for Materials and Environment (LASME), Larbi Ben M'Hidi University, 04000, Oum El Bouaghi, Algeria*

[2]*Research Center in Industrial Technologies CRTI, P.O. Box 64, Cheraga, 16014 Algiers, Algeria.*

[3] *Department of Process Engineering and Petrochemicals, Faculty of Technology, University of Echahid Hamma Lakhdar, P.O. Box: 789, El-Oued 39000, Algeria.*

[4] *Izmir Institute of Technology, Chemical Engineering Department, Gülbahçe Yerleşkesi, Urla İzmir*

[5]*School of Biotechnology,Badr University in Cairo(BUC), Badr City 11829, Cairo, Egypt*

Abstract

Zeolites are essential materials in modern industries due to their uses as cation exchangers, selective adsorbents, and catalysts. In this study,we report novel procedures for producing zeolite T, which is distinguished by its round crystals that closely resemble Saharan flowers. An investigation was conducted on the hydrothermal synthesis of T zeolite in alkaline aqueous solutions without templates. Zeolite T crystals were synthesized via hydrothermal methods with clay-based aluminosilicate gel containing $1Al_2O_3$, $25SiO_2$, $6.5Na_2O$, $2.25K_2O$, and 350 H_2O. Zeolite crystals were formed at a temperature of 130°C, with crystallization durations of 3 and 5 days, respectively, using processed natural bentonite clay as the starting material. A range of analytical methods, such as XRD, FTIR, Raman, SEM, ATD-EDX, BET, ATG, and NH_3-TPD, were used to observe the crystallization stages of zeolite T grains.During the synthesis of Zeolite T, samples were collected at various intervals, with the samples taken after three and five days of reaction being particularly noteworthy. The T1 zeolite is identified as a mixture of T2 zeolite and other impurities present in the reaction medium, indicating that T1 zeolite serves as a precursor phase to T2 zeolite (T1 is a germination phase). The analysis revealed that a treatment temperature of 130 °C for 5 days is optimal. The nucleation of zeolite T from treated bentonite commenced after 3 days. The results indicate that zeolite T2, composed of uniform crystalline grains formed over 5 days, yields a mesoporous structure with a size of 1.35 µm and a molar ratio of 1.78 between molar quantities of silica and aluminum of this zeolite (T Zeolite). An analysis of the BET (surface area) revealed a value of 95.75 m^2g^{-1}, accompanied by a pore volume of 0.010 cm^3g^{-1}. Moreover, the examination of TPD-NH_3 desorption revealed a restricted occurrence of the acidic site of Brønsted, while a significant number of acidic sites of Lewis were detected. The obtained crystalline zeolite T was examined for its ability to catalyze the Hantzsch reaction. In addition, T2 zeolite prepared was used as a catalyst in the synthesis of the 1,1'-(4-(5-bromo-2-thiophenyl)-2,6-dimethyl-1,4-dihydropyridine-3,5-diyl)bis(ethan-1-one) (BTDDB) due to the acidity sites (Lewis and Brønsted acid) in the structure of the zeolite. The result of the reaction has shown a good percentage in the synthetic of BTDDB The results of FTIR, UV, ^{13}C NMR, and ^{1}H NMR spectrum analyses revealed that the structure of the 1,4-dihydropyridine compound was well-defined, and the use of molecular docking and density functional theory (DFT) analysis revealed better performance in the inhibition of the macromolecular targets aminodeoxyfutalosine nucleosidase and DNA gyrase subunit B.

Keywords: Bentonite; Hydrothermal; Zeolite T; Catalysis; Molecular Docking; DFT.

1. Introduction

Since the first synthesis of zeolites in the 1940s by Barrer, these alumino-silicate resources have been extensively utilized for various applications, such as hydrocarbon conversion, size/shape-selective heterogeneous catalysis, gas separation and purification, as well as ion exchange, desiccation, and sorbing methodologies. Crystalline microporous minerals known as zeolites are extensively used as chemical catalysts in many sectors, such as refining oil, basic petrochemistry, and fine chemistry [1]. They exhibit distinct characteristics in terms of activity and selectivity. The primary factors influencing activity

*Corresponding author e-mail: mohamed.ahmed_ali@buc.edu.eg; (**Mohamed A. Ali**).
Received date 30 March 2025; Revised date 01 May 2025; Accepted date 02 June 2025
DOI: 10.21608/EJCHEM.2025.372181.11540

are the Brønsted acid sites of the zeolite and the active metal phase that can be accumulated into the zeolite [2]. Zeolites possess distinct features, such as precise pore sizes, even charge distributions, large specific areas, and significant porosities. These properties render them highly desirable for catalysis, adsorption, pervaporation, and gaseous separation [3].

T zeolite type is a compact crystalline structure formed by the intergrowth of offretite (OFF)-erionite (ERI) zeolite structures, exhibiting strong hydrophilic characteristics. The structural frameworks of the offretite and erionite are distinct yet intricately connected. This phenomenon of stacking defects or intergrowth is frequently observed in synthetic and natural forms of these zeolites, including T zeolite and ZSM-34. The catalytic and adsorbent properties of both erionite and intergrowth-type zeolites of offretite/erionite have been extensively documented in various chemical processes [4]. The zeolite T synthesized by hydrothermal processes is extensively used and is regarded as a standard approach for regulating the pore sizes and crystallinities of target products. Furthermore, several researchers have examined the effects of several parameters, including chemical composition, crystallization duration, and temperature, on the crystal distribution of T zeolite [5].

Metal oxides Al_2O_3, SiO_2, Na_2O and K_2O are used in various fields[6–11], are commonly used for the synthesis and modification of zeolites [12,13]. Many studies have explored the successful synthesis of zeolite T.X.Yin et al They were able to Ultrasonic-pretreated hydrothermal synthesis of less dense zeolite CHA from the transformation of zeolite T[14]. J. Liu et al used the assistance of zeolite seed solution to synthesis of hierarchical zeolite T nanocrystals via a simple and cost-effective process[15]. X. Yin et al. prepared disk-like and pumpkin-like hierarchical zeolite T aggregates, which were also prepared complete the single-template method [16]. S.E. Arshad et al. synthesized a free template of zeolite T from a formulation of metakaolin as a silica-alumina source with low energy consumption while also investigating the influence of temperature and time on hydrothermal synthesis [17]. M. Mirfendereski and T. Mohammadi investigated the effects of hydrothermal synthesis parameters on the structure of zeolite T crystals [4].

Zeolite catalysis has been essential in fossil fuel refinement and the chemical industry. Given the inherent intricacy of catalysis and the unique composition of zeolites, comprehending the essence of zeolite catalysis is exceedingly difficult [18,19]. The research involves the application of several physicochemical methods that, when combined, can yield data on the quantity, dispersion, nature, and intensity of the acid sites (Brønsted and Lewis sites), as well as their correlation with the composition, crystallinity, and structure of the sample. Although kaolin clay provides a vast potential silica-alumina source for zeolitization, the use of natural kaolin clay resources for zeolite T synthesis is a seldom-discussed subject. The primary component of kaolin is kaolinite, a mineral composed of a tetrahedral layer of silica alternated with an octahedral layer of alumina connected by oxygen atoms and hydroxyl groups [20]. The choice of bentonite in this work is based on its possession of Si–O or Al–O octa -tetrahedral sheets. These sheets generate a charge imbalance in the 2:1 layer and make bentonite a promising raw material for the synthesis of zeolites. The optimal method for activating natural clay is to undergo a thermal transformation of the inactive phase into an active phase by calcination method in the presence of alkali hydroxide. This transformation may also be beneficial for later hydrothermal synthesis [21].

The synthesis of 1,4-dihydropyridine prepared from aldehydes, β-ketoesters and ammonia, documented by A. R. Hantzsch in 1881, is the best-known three-component reaction (3CR) [22]. Serval literatures have reported on the synthesis and biological activity of pyridine derivatives[23-25] andalso 1,4-dihydropyridines via heterogeneous catalysis, employing an important type of zeolite site (Brønsted or Lewis) used as a heterogeneous-acid catalyst for different petroleum methods and organic syntheses because of its selectivity as a catalyst catalytic [26,27]. These catalysts have affected the attention of organic chemists owing to their attractive features, such as small amounts of catalyst, recyclability, reusability and tolerance to metal leaching into solution [28].Contrary to what was stated in previous literature the novelty of this study the synthesis of zeolite derived from treated bentonite clay, marking the inaugural investigation of this specific type of zeolite.

In this work, we developed a bentonite clay route to synthesize small zeolite T crystals with a catalytic application. The synthetic conditions of zeolite, such as the stirring time and ultrasonic system, were directly associated with the success in a highly crystalline T2 zeolite, and the roles of the zeolite in the catalysis reactions, crystal growth kinetics, and crystallization behavior in the ultrasonic system were investigated in detail. These materials are reported to be very attractive as catalysts and adsorbents for many chemical methods (catalytic cracking, organic synthesis). The zeolite used in the catalytic reaction of Hantzsch, because of its acidic sites and structure, is determined by several methods of analysis. The 1.4hydropyridine product results from the synthesis of 5-bromo-2-thiohydroxyaldehyde. We extended our research on the use of 1,4-dihydropyridine in investigations of molecular docking.

2. Materials andmethods

2.1. Materials

The reactive include precipitated silica (SiO_2, 99.8 wt%, Aldrich), sodium hydroxide pellets (NaOH, 99 wt%, Merck), and potassium hydroxide (KOH, 85 wt%, Merck), all sourced from Aldrich Sigma. The composition of bentonite clay, which serves as an aluminum source. Additionally, the materials comprise 5-bromo-2-thiophenecarboxaldehyde (C_5H_3BrOS, 95%, Sigma Aldrich), 2,4-pentadione ($CH_3COCH_2COCH_3$, 99%, Sigma Aldrich), ammonium hydroxide (NH_3, 30%, Sigma Aldrich), ethanol (≥96%), dichloromethane (DCM; anhydrous, ≥99.8%, Sigma Aldrich), and deionized water.

2.2. Treatment of the Bentonite

Bentonite clay served as the local source of silica and alumina in this study. It was collected from the mountains at Bir ElAter, Tebessa-Algeria; it was dried at 100 °C for 2 days and then crushed and sieved to obtain 45 µm grains. The 45 µm clay was mixed with 50% sodium carbonate and was treated at 800 °C in air for 2 hours in a muffle furnace to dissolve the quartz grains [29]

2.3. Preparation of T zeolite

Fig. 1 shows the steps of the synthesis of zeolite T. Sodium Hydroxide and Potassium Hydroxide, treated bentonite, and silica gel were mixed with deionized water to obtain a synthesis mixture with a molar composition of $1Al_2O_3$, 25 SiO_2, $6.5Na_2O$, $2.25K_2O$, and 350 H_2O [4].

Fig. 1: Synthesizing zeolite T.

Under vigorous stirring at ambient temperature for 15 minutes, Sodium Hydroxide and Potassium Hydroxide were mixed in deionized water until all the pellets dissolved. Treated bentonite was added gradually (to the alkaline solution prepared above) and mixed strongly. The mixture was agitated for 1 hour to complete the mixing. In the second step, under slow stirring, the silica gel was added to the solution in a small amount and slowly stirred until it was complete; then, it was continuously stirred for 3 hours to achieve a homogeneous solution, and the mixture was stirred at 30 °C for 24 hours. Finally, before the crystallization process began, the gel mixture was pretreated via ultrasonication for 90 minutes to produce a homogeneous gel. The homogeneous gel was transferred into an autoclave (Teflon-lined stainless steel) and kept in a 130 °C oven (MuellerIsotemp Oven) for 180 h and 323 h. After that, the autoclave was removed from the oven to halt the crystallization method. The resulting crystals were filtered and washed with distilled water. Finally, the solid crystals that formed were dried in a vacuum oven at 130 °C for 3 hours.

2.4. Synthesis of 1,1'-(4-(5-bromo-2-thiophenyl)-2,6-dimethyl-1,4-dihydropyridine 3,5-diyl)bis(ethan-1-one) (BTDDB)

A mixture containing of ammonium hydroxide (20 mmol), 5-Bromo-2-thiophene carboxaldehyde (15 mmol), pentane-2,4-dione (15 mmol), and 35 mg of H-T2 zeolite (prepared by stirring zeolite T2 with NH_4Cl for 24 hours and subsequently heating at 500°C) was exposed to stirring in a reflux system at 75°C for 7 hours. The progress of the reaction was monitored using a mix of n-hexane and ethanol, to separate the point of the product 1,1'-(4-(5-bromothiophen-2-yl)-2,6-dimethyl-1,4-dihydropyridine-3,5-diyl)bis(ethan-1-one) in the CCM test's from the total solution obtained in the

reaction, We mixed 1 ml of ethanol and 9 ml of n-hexane to reduce the polarity of the ethanol solvent. Upon completion, 10 mL of ethanol was added and heated to dissolve the resulting product, followed by the introduction of methylene chloride to induce precipitation of white crystals. The crude product was filtered, washed with methylene chloride, and dried. Recrystallization from methanol resulted in the isolation of the pure product. After solvent evaporation, 10 mL of CH_2Cl_2 was added to recover the catalysts. The yield obtained was 0.2 g (70%), and the product was characterized as a white powder with a melting point of 187-188°C. Fig. 2 shows the chemical reaction for the synthesis of 1,1'-(4-(5-bromothiophen-2-yl)-2,6-dimethyl-1,4-dihydropyridine-3,5-diyl)bis(ethan-1-one)[22].

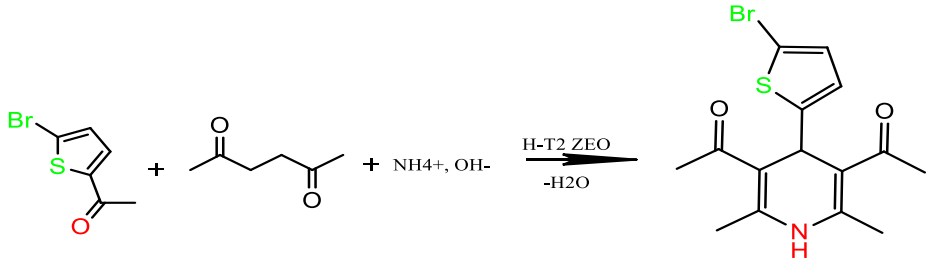

Fig. 2: The chemical reaction for synthesis of BTDDB

2.4. Characterization

Muffle NABERTHERM MODE II was used to heat the bentonite clay and calcine, and ultrasonic SONOREX SUPER RK 106 waves at a frequency of 60 kHz were used to prepare a homogenous solution. The characterization of the product has been performed via many methods. First, the chemical element of the synthesized product was evaluated via elemental analysis using a Bruker S8 LION system. A pellet of clay and treated clay with a diameter of 3 0.5 cm and a mass of 10 g was prepared to define the chemical composites present in the clays. The bentonite and bentonite-treatedsamples were subsequently characterized via an X-ray diffractometer system (XRD, BRUKER-binary V3 (.RAW)) with Cu Kα radiation (λ=1,54060 Å). XRD was measured for 2θ values ranging from 5° to 88° at a scan step time [s] of 2. The T1 and T2 zeolite phases were analyzed by X-ray EMPYREAN intelligent diffractometer system (XRD, EMPYREAN, Malvern Panalytical) with Cu Kα radiation (λ=1,54060 Å).

Diffraction angles were reflected for 2θ values ranging from 5° to 60° at a scan step time [s] of 147.3900. The morphology and grain size were observed by scanning electron microscopy with a Thermo Scientific (TM Quattro) scanning electron microscope functioning at 5 kV; the distribution elemental was measured via energy-dispersive X-ray spectroscopy (EDXS) attached to a scanning electron microscope. The results of the thermal analysis experiments were studied via a combined analyzer TGA/DrTGA (Detector TGA-51).

The T zeolite was heated in a current of nitrogen (60 mL/min) at 10 °C/min from room temperature to 1000 °C. Specific surface area, pore volume, and pore size were plotted via Brunner-Emmett Teller (BET), t-plot, and Barrett–Joyner–Halenda (BJH) methods via a Micromeritics Instrument Corp. (Gemini V2.00, 2150). The infrared typical vibration bands at 400–4000 cm^{-1} were measured by a Fourier transform infrared spectrometer (FTIR-4700, Jasco). Raman was used to determine the vibrational types of the molecules and to indicate their Brønsted and Lewis acidity, which were detected by a Raman - Minerals (FT) – HORIBA Fourier transform infrared spectrometer (FTIR QS300). The programmed desorption of NH_3 (TPD-NH_3, Micro-Active for Auto-ChemII 2920 version 6.01, Serial # 205, Unit 1) was used to measure acidity.

The zeolite wasexposed to NH_3 at 0–500 °C with a heating rate of 10 °C/min and a gas flow rate of 50 mL/min. TPD-NH_3 experiments were executed as follows: first, 144.1 and 133.1 mg of adsorbent zeolite were treated under helium flow (50 mL min^{-1}) and heated to 500 °C (5 °C min^{-1}) for 3 h. Then, ammonia diluted for 30 min in He flowed through the sample at 100 °C until saturation, which was identified by a mass spectrometer. Finally, ammonia was desorbed by switching the flow to He and heating the sample to 500 °C (10 °C min^{-1}). Nuclear magnetic resonance was used to identify the organic products obtained from the Hentzch reaction, with UV and FTIR analyses.

3. Results and discussions

3.1. Synthesis of T zeolites expanding diverse crystallization times

3.1.1. FTIR of Bentonite and Treated Bentonite

FTIR spectroscopy is a significant method employed for identifying functional groups that are characteristic of the adsorbent's surface [30] using a coupled Fourier transform spectrometer, and a digital calculator allowing the tracing of the spectra between [4000 and 400 cm^{-1}], with a "Cary 600 Series FTIR Spectrometer" brand device. These groups are often responsible for the bonds. Fig. (3) Shows the FTIR spectra of the Bentonite and Treated Bentonite.

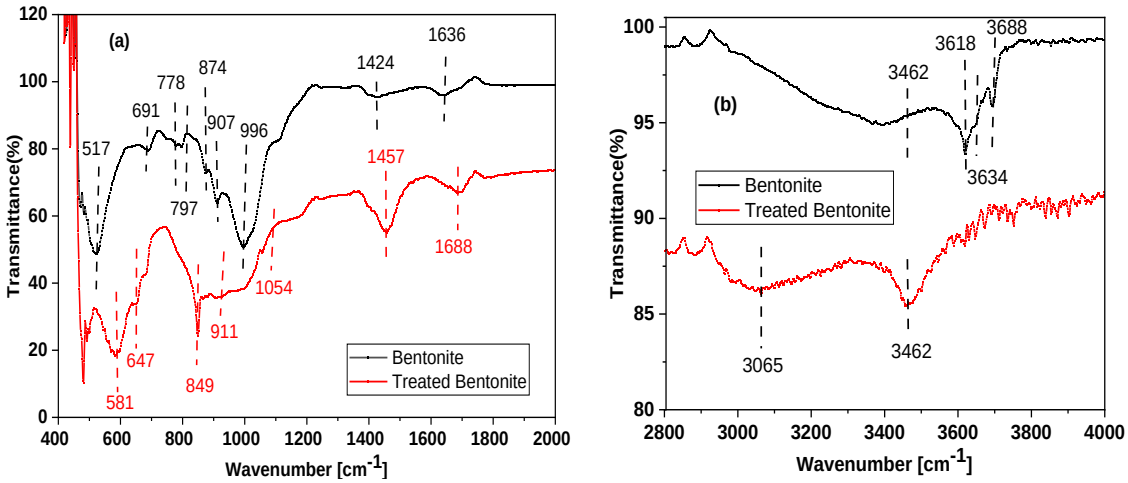

Fig. 3: IR spectra of the Bentonite and Treated Bentonite (a): λ=400-2000 $cm^{-1}$and (b): λ=2800-4000 cm^{-1}

The arrangement and form of these bands are strongly affected by the characteristics of the octahedral atoms to which the OH groups are connected. The absorption bands observed at approximately 3634 cm^{-1} in all measured spectra of montmorillonites are characteristic of dioctahedral smectite, with a significant proportion of aluminum (more than 50%) in octahedral positions. This vibration corresponds to the stretching of hydroxyl groups within the structure and is accompanied by a bending vibration at approximately 907 cm^{-1} involving Al-Al-O. For trioctahedral minerals, the OH stretching vibrations in the structure are shifted to higher frequencies, often falling within the bands of 3618, 3634 to 3688 cm^{-1}. The infrared spectra verified the existence of water deformation vibrations and carbonate trace O–H absorption bands at 1636 cm^{-1}. and 1421 cm^{-1}, respectively, is feasible [31]. The band at 996 cm^{-1} is associated with a stretching vibration occurring within the plane of the Si–OH bond. The presence of distinct and intense peaks at 797 and 778 cm^{-1}, together with a less prominent peak at 695 cm^{-1}, in the spectra of bentonite indicates the existence of quartz. The presence of the adsorption band at 518 cm^{-1} is associated with the Al-O-Si deformation of montmorillonite. The mineral phase is predominantly composed of montmorillonites, as shown by the presence of absorption bands at 3634, 907, and 518 cm^{-1}[32]. The wide spectral range centered at 3462 cm^{-1} is caused by the stretching vibrations of OH groups in water molecules that are hydrogen-bonded. On the other hand, the smaller peak at 3065 cm^{-1} is associated with the suggestion of the water bending vibration, which is accountable for the broader peak observed at 1684 cm^{-1}[33]. The 911 cm^{-1} band is a result of the Al–Al–O bending mode, whereas the 1055 cm^{-1} shoulder adsorption band is attributed to the Si–O stretching mode [32]. The carbonate band of Na_2CO_3 at 1457 cm^{-1} coincided with the doublet feature specific to amorphous $CaCO_3$.

The out-of-plane deformation mechanism of carbonate likely causes the 849 cm^{-1} band. The presence of quartz is shown by the bands at 778 cm^{-1} and 797 cm^{-1}. The absorption band at 641 cm^{-1} is caused by out-of-plane Al–O–Si vibrations, whereas the bands at 581 cm^{-1} are associated to Al–O–Si and Si–O–Si bending vibrations. When the clay is heated with 50% sodium carbonate, the final product is a white powder. This powder is easily dispersed and is composed of a combination of sodium silicate and alumino-silicate of sodium phases [29]. The properties of octahedral atoms have a substantial effect on the organization and shape of absorption bands in both processed and unprocessed materials. The distinction between dioctahedral and trioctahedral minerals is based on the specific vibrations associated with OH stretching and bending. The infrared spectra also revealed the presence of water and carbonate residues. The lack of clearly visible quartz bands in the treated clay sample indicates the possible removal of quartz during the treatment procedure. Moreover, the modifications caused using sodium carbonate suggest changes in composition.

3.1.2. FTIR of the Zeolite

Fig. 4: Shows the FTIR spectra of the zeolite. In the spectrum range of 4000 to 3200 cm^{-1}, three principal absorption bands are discernible, attributed to various hydroxyl groups constituting the Brønsted acid site (BAS). These hydroxyl types are differentiated based on their spectral characteristics and association in hydrogen bonding. The first type resembles an exceptional BAS with an OH vibrational frequency ranging from 3620 to 3646 cm^{-1}.

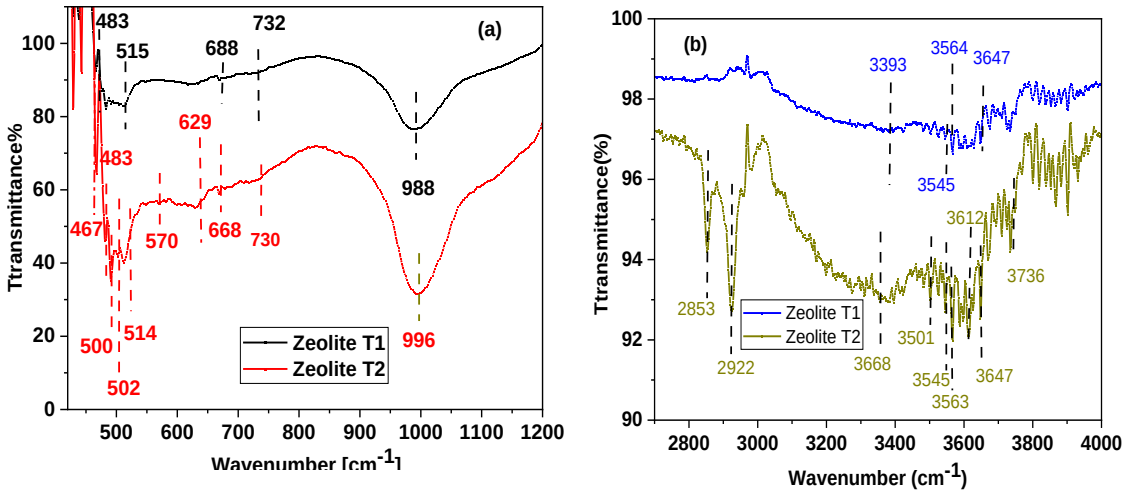

Fig. 4: IR spectra of the zeolite T1 and T2 (a): λ=420-1500 cm^{-1} and (b): λ=2700-4000 cm^{-1}

A weak adsorption band at 3647 cm^{-1} is observed for zeolites T1 and T2, with T2 exhibiting an additional absorption band at 3613 cm^{-1}. The second type of BAS pertains to hydroxyls with bands in the 3400–3600 cm^{-1} region. Zeolite T1 displays two bands at 3393 and 3545 cm^{-1}, whereas zeolite T2 exhibits three bands at 3501, 3545, and 3562 cm^{-1} (Fig. 4. b). These associating hydroxyls are not involved in regular hydrogen bonding, which is characterized by nearly linear O-H…O arrangements.

The third type of BAS corresponds to hydroxyls with linear hydrogen bonds to oxygen centers opposite the zeolite ring, typically exhibiting an O-H band between 2950 and 3230 cm^{-1}[34]. While Zeolite T1 lacks bands in this region, Zeolite T2 presents three bands at 2853, 2922, and 3368 cm^{-1}. The most intense vibration in the950–1250 cm^{-1} region is attributed to stretching of T-O, which primarily involves the motion of oxygen atoms and is designated as an asymmetric stretching mode ←OT→ ←O. In Fig. (4. a) Zeolite T1 shows a band at 996 cm^{-1}, whereas zeolite T2 displays a band at 994 cm^{-1}.

The subsequent strong band, within the 420–500 cm^{-1} range, is assigned to the T-O bending mode. Zeolite T1 has two absorption bands at 465 and 483 cm^{-1}, whereas zeolite T2 has three absorption bands at 467, 483, and 500 cm^{-1}. Symmetric stretch modes are categorized into internal tetrahedron stretches (650–720 cm^{-1}) and external linkage symmetric stretches (750–820 cm^{-1}), reflecting structure-sensitive external linkages. Zeolite T1 exhibited a band at 732 cm^{-1}, and zeolite T2 presented two bands at 668 and 730 cm^{-1}. Fundamental tetrahedral modes in silica include the Si-O asymmetric stretching mode from 800–1100 cm^{-1}, the Si-Si symmetric stretching mode from 600-800 cm^{-1}, and the bending and distortion modes below 600 cm^{-1}. Additionally, the appearance of the band of the stretching mode of the double ring at 500–650 cm^{-1} and the bending or distortional mode of the “pore opening" at 300–420 cm^{-1} are noted [35]. Zeolites T1 and T2 show three bands at 502, 514, and 629 cm^{-1}, with zeolite T2 displaying a fourth weak band at 570 cm^{-1}. Ultimately, Zeolite T2 displays supplementary absorption bands in comparison to those of T1, suggesting differences in the arrangement of the hydroxyl groups and structural properties.

T2 exhibited heightened vibrational modes within the 950–1250 cm^{-1} and 420–500 cm^{-1} ranges, indicating variations in T–O strains and bending modes. These differences offer a valuable understanding of their varied structures and possible applications.

3.1.3. Raman of the treated bentonite clay

Raman of treated bentonite clay allows to characterization of the structural and chemical modifications of this clay after treatment. Depending on the type of treatment applied, the bands in the Raman spectrum can change in intensity, position, or shape. Fig. 3 shows Raman spectra of treated bentonite.

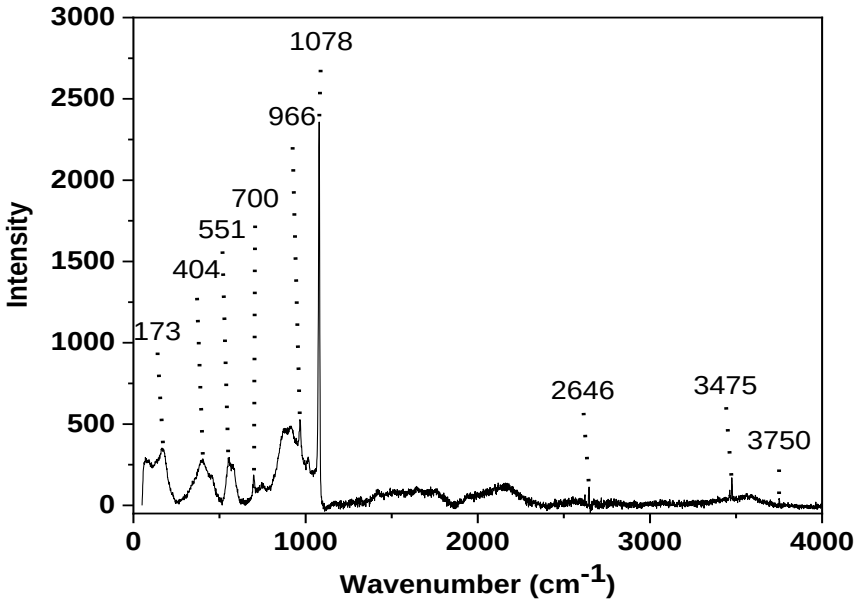

Fig. 5: Raman spectra of treated bentonite.

The significant peak at 966 cm^{-1} in the spectrum of Na-bentonite is caused primarily by the symmetric stretching vibration of Si-O, where O-H represents nonbridging oxygen. This peak also indicates that the original clay is a dioctahedral phyllosilicate, as shown by the presence of Raman peaks ranging from 800 and 1100 cm^{-1}, according to previous reports. The presence of OH/H_2O vibrational modes in the spectra of Na-bentonite is further validated by the peaks observed within the 3750, 3475, and 2646 cm^{-1} ranges [36]. The intense Raman peak observed at 700 cm^{-1} is a result of the vibrations of SiO_4 units. Additionally, the larger feature observed at approximately 404 cm^{-1} is attributed to the bending vibrations of M-OH bonds, as well as the bending modes of Si-O-Si (Al) bonds.

The high-intensity band at 551 cm^{-1} changed. The location of the prominent peak at approximately 174 cm^{-1} changes depending on the type of clay mineral. This is likely caused by the presence of SiO_4 and is impacted by the substitution of Al as well as the dioctahedral or trioctahedral nature of the mineral.

The most intense carbonate band is detected at approximately 1078 cm^{-1} and is present only slightly in the carbonate admixture found in treated bentonite [37]. Typically, the existence and specific type of cation interlayer can be determined by observing bands with frequencies below 100 cm^{-1}, which correspond to the vibration of the interlayer cation. Additionally, the bands at approximately 280 cm^{-1} indicate the bending of the O-H-O triangle.

Based on the literature, both sodium and calcium cations in the interlayer produce a band vibration at approximately the same wavenumber of 69 cm^{-1}.

Therefore, the only way to distinguish between these two cations is by observing the O–H–O bending band. The replacement of octahedral central atoms can be inferred from the spectrum range of 785–915 cm^{-1}, which corresponds to deformations in vibrations. The spectral band related to the bonding of O–H with octahedral cations, specifically Al-Al-OH, is detected at a frequency of 915 cm^{-1}[32]. The lack or decrease in carbonate bands in the treated bentonite samples suggests that the treatment may have caused changes in the material.

An especially remarkable observation is the possible removal of quartz from the treated bentonite, as evidenced by alterations in the spectrum characteristics. Furthermore, observations at lower frequencies offer valuable information about the composition of cations between layers and the substitutions that occur in octahedral atoms.

3.1.4. Raman spectra of the zeolite

Fig. 6 shows Raman spectra of zeolites (a): T1 and (b). T2. The hydroxyl groups exhibit antisymmetric and symmetric stretching vibrations, which are observed in the 3700-3420 cm^{-1} spectral range. The infrared spectra exhibit a high intensity, but the Raman scattering spectra show a low intensity; this is consistent with what was cited in the Ref [38].

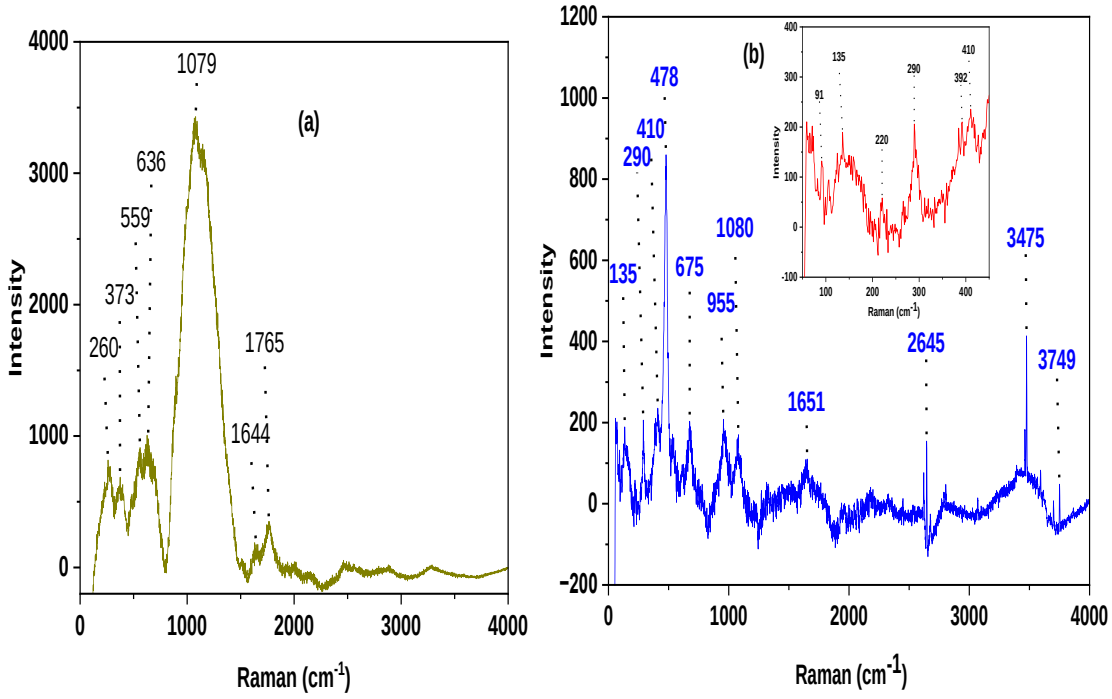

Fig. 6: Raman spectra of zeolites (a): T1 and (b): T2.

The frequencies corresponding to the translational mode of the Na– O bonds can be observed in the far-infrared and Raman spectra within the wavenumber range of 218-163 cm^{-1}. According to*P. M. Kester et al*, the wavenumbers below 163 cm^{-1} in this study can be attributed to water-cation complex vibrations and the translational modes of K– O bonds [39]. The spectra include a prominent peak at approximately 3750 cm^{-1}, corresponding to silanol groups Si – OH. Additionally, two peaks detected at 3590 and 3698 cm^{-1} indicate the stretching vibrations of acidic Brønsted OH groups Si – O(H) – Al.

Furthermore, a minor peak at 3650 cm^{-1} is observed, corresponding to the stretching vibrations of OHgroups connected with minority extra framework Al sites. Stretching characteristics were observed at approximately 3590 cm^{-1} and 3698 cm^{-1}, which can be attributed to the presence of protons in the sodalite cages and super cages, respectively [40]. The zeolite T1 (Fig.6. a) exhibited three distinct major ring structures detected at 260, 373, and 559 cm^{-1}.

These structures were identified as vibrations of eight-membered, six-membered, and four-membered rings [41]. Fig. 6 (b) shows three distinct primary ring configurations found in Zeolite T2. The vibration of four-membered rings is considered by a prominent band at 478 cm^{-1}, accompanied by a secondary band at 533 cm^{-1}.

The bands observed at 290 cm^{-1}, 392 cm^{-1}, and 410 cm^{-1} correspond to the bonding of structural units that occurs during the crystallization process of six-membered rings. The third absorption bands at 218 and 265 cm^{-1} correspond to the vibrations of eight-membered rings. Consistent with prior research on zeolite T, the bands observed at 675 cm^{-1} in sample T2 were attributed to stretching symmetric modes of T– O bonds involving T – Si or Al atoms. In contrast, the bands at 955 and 1080 cm^{-1} were attributed to asymmetric stretching modes.

The bands at 955 cm^{-1} and 1085 cm^{-1} were associated with lattice oxygen in the skeleton [40]. The band at 636 cm^{-1} in sample T1 was attributed to T– O stretching symmetric modes, whereas the band at 1079 cm^{-1} was attributed to stretching asymmetric modes.

3.1.4. XRD of bentonite and treated bentonite

Bentonite is characterized by a specific crystal structure that can be analyzed by X-ray diffraction (XRD). Fig. 7 displays the XRD analysis of bentonite and treated bentonite, along with the simulated XRD powder patterns of silicon oxide.

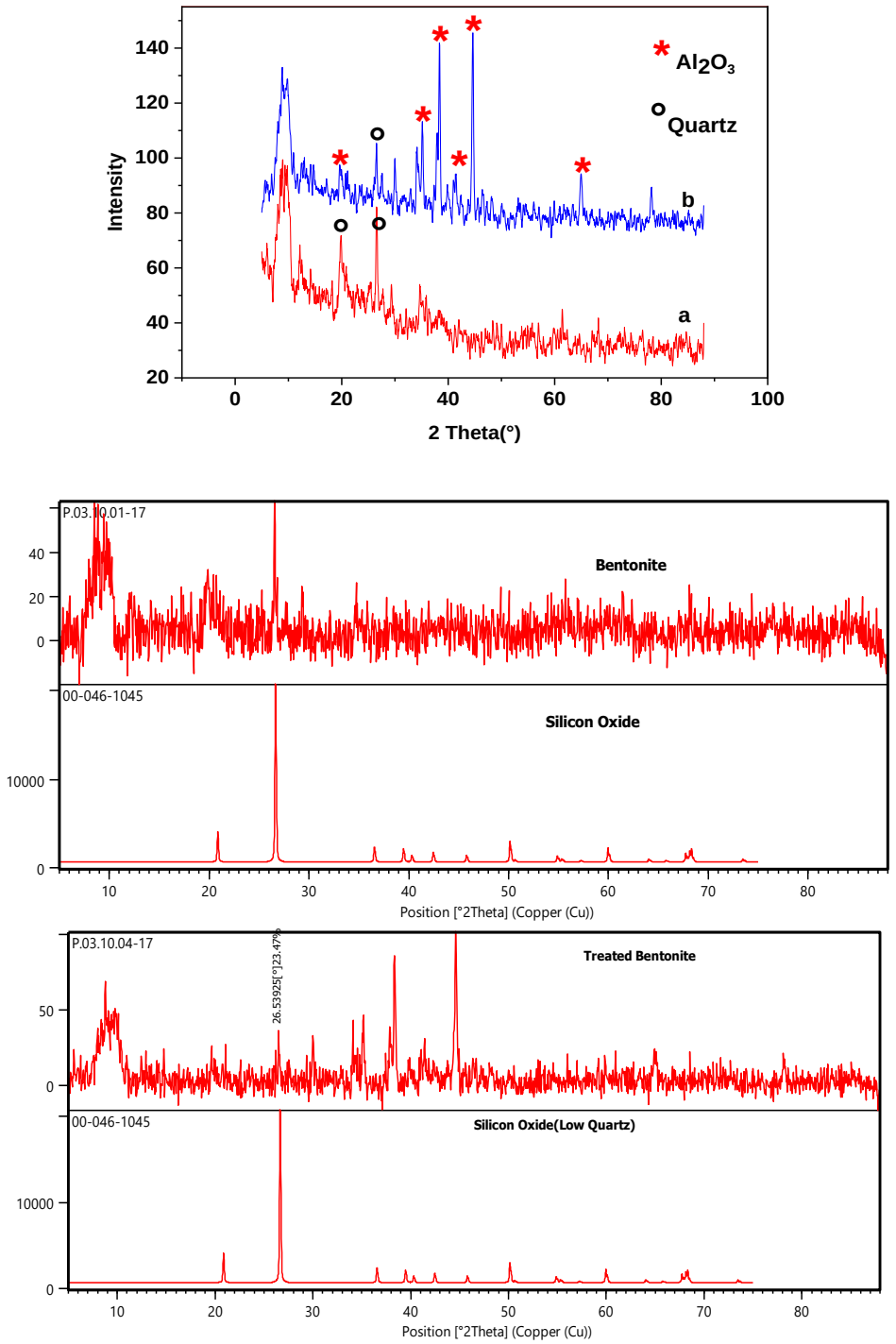

Fig. 7: XRD analysis of bentonite(a) and treated bentonite(b) with the simulated XRD powder patterns of silicon oxide.

Quartz reflection is observed at 3.35 A°. The quartz concentration of the treated bentonite significantly decreased. The analyzed bentonite sample exhibited (001) and (002) reflections of kaolinite at 7.22–3.52 A°, respectively. These reflections vanish when the sample is subjected to heating at 800 °C [42]. The d_{001} assessment of the basal montmorillonite reflection in the original clay is 14.9 A°. Immediately upon activation, the primary reflection aligns most closely with d_{001} ~ 15.47 A°, with a secondary peak at 12.92 A°, suggesting that some calcium cations were substituted with Na^+. After calcination, the comparative intensity of the shoulder corresponding to the Na-form increased. The cation exchange process quickly occurs when a large amount of Na_2CO_3 is used. As a result, the material studied immediately after the exchange only displays the basic reflection characteristic of the Na-form of montmorillonite. The XRD pattern remains unchanged after a

long aging period [33]. The new peaks of oxide aluminum [43] are shown in the treated bentonite with a (2θ=35.21, 38.3, 41.4 and 44.55°).

3.1.6. XRD of the zeolite

Zeolite T is a crystalline aluminosilicate belonging to the zeolite family. It is characterized by a specific crystal structure that can be analyzed by X-ray diffraction (XRD). The X-ray diffraction pattern of zeolite T shows characteristic peaks corresponding to the lattice planes of its crystal structure. These peaks allow to the identificationof the crystalline phase and confirm the purity of the material. Fig. 08 (a, b) shows XRDspectra of the T1 and T2 zeolites with the simulated XRD powder patterns of offretite and erionite.

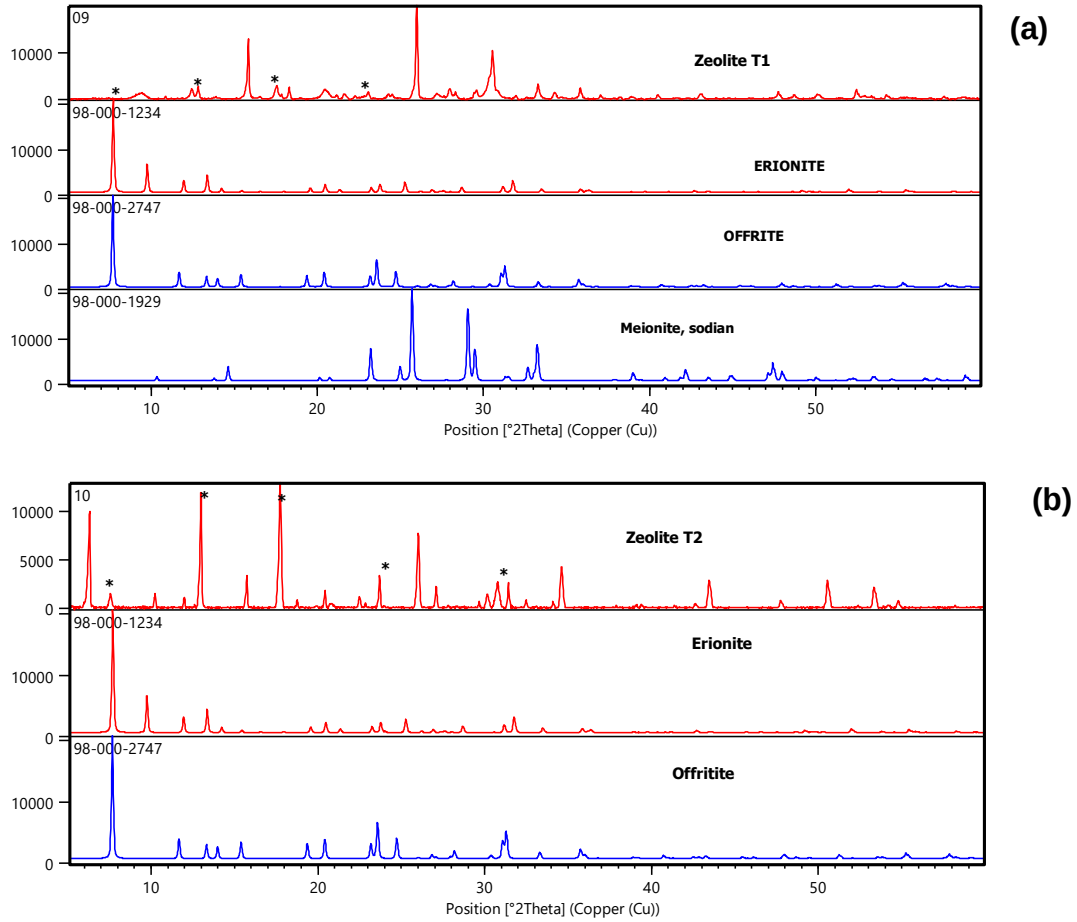

Fig. 8: XRD spectra of T1 and T2 zeolite nanoparticles with the simulated XRD powder patterns of offretite and erionite.

The pattern displayed represents a phase of crystalline offretite, which is a well-known zeolite structure. The XRD powder pattern of the offretite can be observed, andthe product exhibited high crystallinity and was devoid of impurities, as evidenced by the low baseline and the presence of offretite peaks. Nevertheless, there is a significant discrepancy in the relative magnitudes of several peaks between the two patterns. Furthermore, the peak sites of T1 zeolite and T2 zeolite consistently shift toward higher two theta values. The arrangement of cancrinite cages between hexagonal prisms (double 6-membered rings) distinguishes the architecture of offretite and erionite [44,45]. The erionite XRD pattern exhibits d-spacings comparable to those of offretite. However, erionite also displays additional reflections, as highlighted by the asterisks in Fig. 6 (b) of T2 zeolite. These reflections are too weak to be clearly distinguished in the XRD pattern of the zeolite product synthesized by the present method. These data suggest that the product's crystals consist primarily of offretite, with minimal or negligible stacking faults originating from erionite sheets. Adding potassium ions to the synthesis mixture can shift the resulting phase from omega zeolite to offretite, clearly illustrating the importance of potassium cations in driving the structural development of offretite. After approximately 3–5 days, the mixture synthesis underwent crystallization, forming aphase of the offretite. The process of offretite phase crystallization generally ends within approximately five days [43]. The XRD patterns of all the zeolite closely correspond to the XRD pattern of the T zeolite structure documented in the literature [3]. T1

Zeolite and T2 exhibited the distinctive peaks observed in T2 zeolite at 2θ values of 7.56°, 12.98°, 17.74°, 20.79°, 23.69°, and 31.5°. The T1 zeolite signal has a significantly lower strength. The intense signal observed at a 2θ angle of 17.74° with a (111 reflection: d~ 4.99A°) at T2 zeolite is attributed to the Offretite phase. The results demonstrate the effective synthesis of T zeolite by applying sono-chemical-assisted pretreatment and growth hydrothermally. The amorphous phase is exclusively detected in T1. The weak XRD peaks at T1 zeolite at 2θ = 7.5, 23.6, and 17.49° suggest a limited quantity of zeolite T crystals and an incomplete conversion of zeolite T crystals. T2 zeolite has a greater peak intensity than does T1 zeolite. The outcome suggests that longer hydrothermal growth durations increased from 3 to 5 days, resulting in the formation of more stable crystalline phases of T2 zeolite. This was observed while maintaining a consistent sonochemical-assisted pretreatment duration of 90 minutes. Thus, a hydrothermal growth duration of 5 days is necessary to achieve complete crystallization of zeolite T (T2). Furthermore, as depicted in Fig. 6, a hydrothermal growth period of 3 days had a minimal effect on enhancing the crystallinity of zeolite T (T1). Therefore, it can be deduced that subjecting zeolite T to pretreatment for 90 minutes via sonochemical assistance and a hydrothermal growth period of 5 days results in the desired completely crystalline zeolite T (T2) [46].

3.1.7. Morphologicalstudy

Micrographs of the treated bentonite clay, T1 and T2 zeolite are shown in Fig 9. SEM analysis of treated bentonite clay revealed compact and mono dispersed spherical grains of variable sizes of the order of 5 µm, these grains have a rough surface (Fig. 9 a).

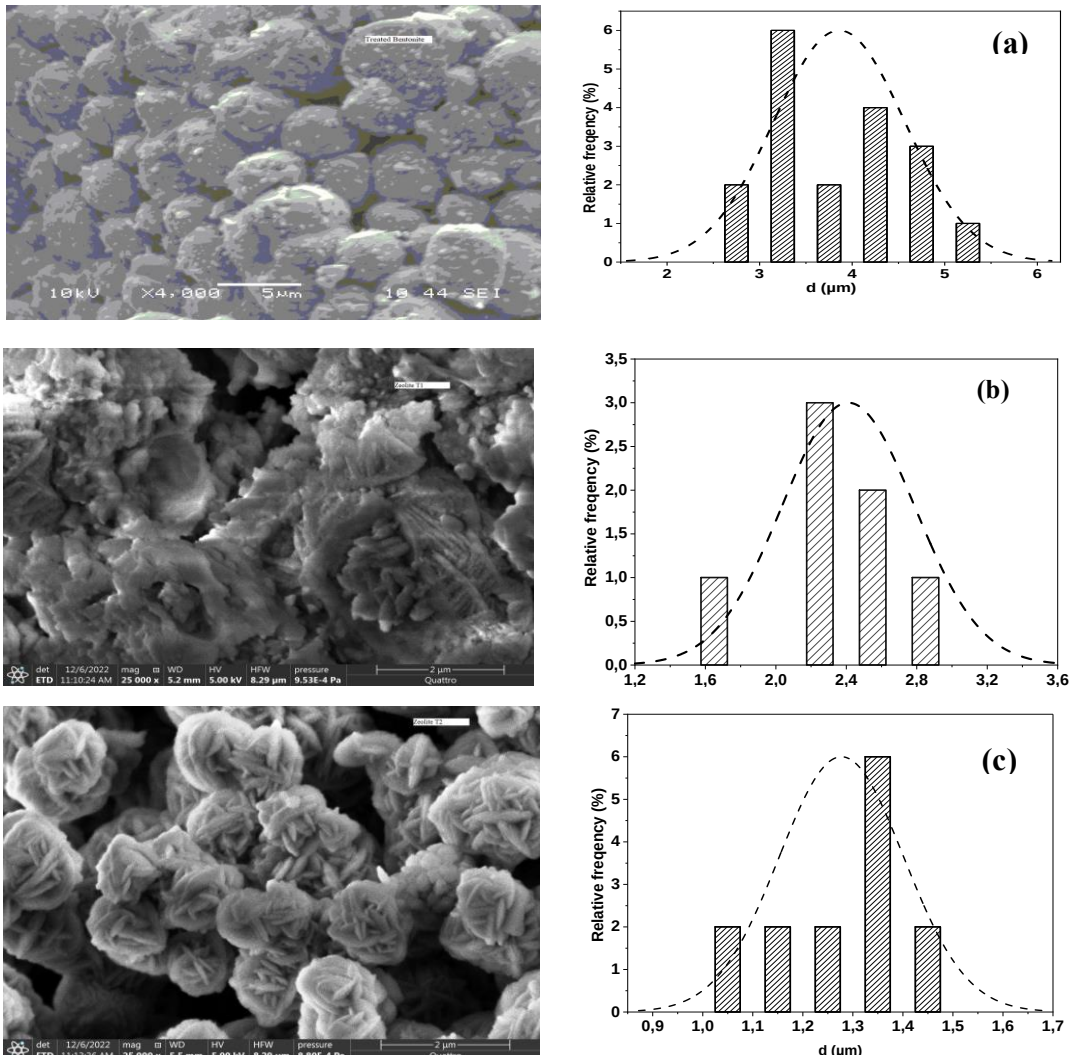

Fig. 9: Scanning electron microscopy (SEM) analysis of: (a) Treated Bentonite clay, (b) T1 zeolite (c) zeolite T2.

Fig. 9.b represents the SEM image of zeolite T1, it shows a different morphology to that of bentonite clay (Fig. 9. a). Various morphologies and amorphous substances are noted. Large tiny particles (about 0.2 µm) on the surface indicate that the formation of crystals occurred naturally and energetically by the combination and accumulation of small particles. The SEM image of zeolite T2 (Fig.9 c) shows a different morphology from those shown in Fig. 9 revealed the existence of large faceted spherical crystals resembling Saharan flowers, measuring 1.3 µm. These crystals are representative of zeolite T2. In addition, tiny crystals were observed, which are probably treated as bentonite clay used as a substrate for the preparation of zeolite. The aspect ratio of the crystal increased as the reaction time increased. The prolonged duration of zeolite crystallization significantly influenced the average grain size of the crystals. The particle size was approximately 2.25 µm (Fig. 9).This is agreed with those presented in the XRD and Raman analysis. In summary, the SEM analysis offers valuable information regarding the unique morphological characteristics observed in the treated bentonite clay, T1 and T2 zeolite configurations. In the treated bentonite clay structure, spherical grains form globular structures, whereas the T1 zeolite structures are composed of micro-flowers, micro-sheets, and non-spherical grains within micropores. Additionally, the T2 zeolite exhibits a greater particle density compared to the T1 zeolite structure. Furthermore, the investigation of T2 zeolite structures evolves from micro-flowers and pores to micrometric plates and aggregated spherical particles.

3.1.8. Compositional analysis

The elemental analysis of zeolite T1 and T2 particles was conducted via dispersive energy X-ray spectroscopy (EDS), as shown in Figures 10 (a, b). The study revealed Si/Al and Na/Al ratios of (0.56, 0.26) and (1.78, 1.42) for zeolites T1 and T2, respectively. These ratios confirm that the composition of sample T2 corresponds to zeolite T [20]. Tables 1 and 2 display the results of the EDS study. T1 Zeolite has an EDS spectrum (Fig. 8. a and b), representative the presence of Al, Si, and O. The EDS analysis results in the data (Fig.10 a) indicate that T1 zeolite has the highest percentage of oxygen, followed by aluminum, and the lowest percentage is in silicon [47]. Additionally, the presence of calcium and magnesium can be attributed to impurities found in the treated clay. The EDS spectrum of T2 in Fig. 10 (b) indicates the presence of Al, Si, and O. The data reveal that this T zeolite has the maximum oxygen content, followed by silicon and sodium. Conversely, aluminum has the lowest content, whereas calcium and magnesium are absent, suggesting that the treated clay has undergone a complete reaction.

Table 1: EDS study T1 Zeolite

Element	Weight (%)	Atomic (%)
O	48.07	56.02
Na	5.43	4.34
Al	19.99	13.82
Si	11.34	7.53
K	3.95	1.88
Ca	0.62	0.29
Mg	0.76	0.58

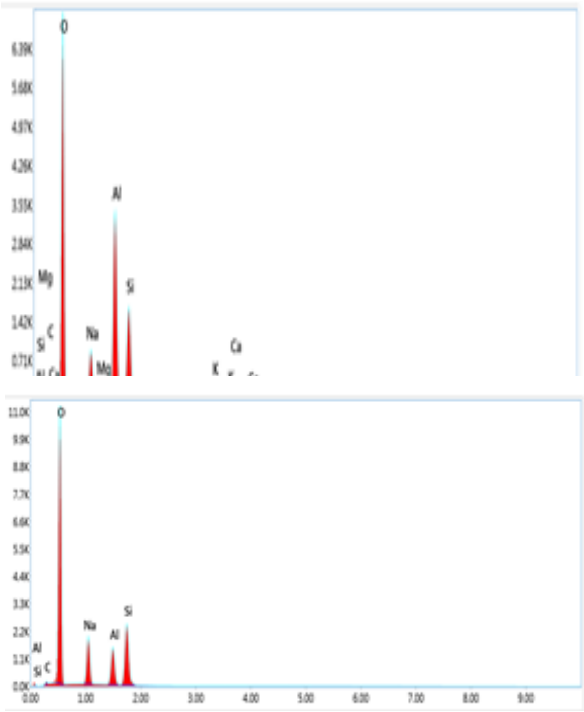

Table 2: EDS study T2 Zeolite

Element	Weight (%)	Atomic (%)
O	57.80	65.06
Na	11.95	9.37
Al	8.39	5.60
Si	14.97	9.60

Fig. 10: EDX spectrum of (a) : T1 and (b): T2 zeolite.

3.1.9. BET analysis

Fig. 11 shows the adsorption nitrogen and desorption isotherms of the T1 zeolite and T2 crystals synthesized at 130 °C for 3 and 5 days, respectively. The micropores were rapidly absorbed at approximately p/p_0 = 0.30 within a reaction time of 3 and 5 days. Once the relative pressure reached approximately 0.77, there was a significant rise in the rate at which nitrogen was absorbed. The data exhibit an IUPAC type IV isotherm, with the hysteresis loops attributable to the realization of textural mesoporosity caused by the intergrowth of the crystals [20].

The Type IV isotherm is distinguished by its hysteresis loop, which arises from capillary condensation in mesopores, and the peak adsorption capacity at elevated p/p_0 values. The initial portion of the Type IV isotherm is attributed to monolayer–multilayer adsorption because it closely matches the corresponding portion of a Type II isotherm obtained via the specified adsorption on the same surface area of the adsorbent in a nonporous situation [48].Table 3 indicates that as the duration of hydrothermal growth increases from 3 to 5 days, the surface area increases from 88.43 to 95.74 m^2/g. Generally, the Langmuir surface area exceeds the BET surface area.

Table 4 indicates that the surface areas of zeolite T2 are greater than those of zeolite T1. Additionally, the data reveal that the mesopore volume of zeolite increased starting 0.003 cm^3/g for T1 zeolite and 0.010 cm^3/g for T2 zeolite. However, it is value observing that the average pore diameter for zeolite T1 is greater than that for zeolite T2. The increase in surface area is appropriate primarily to the developed crystallinity of zeolite as the hydrothermal progress period increases. This finding is consistent with the XRD patterns observed for zeolites T1 and T2, as shown in Fig. 8. The peaks intensity corresponding to the crystallinity of zeolite T increases as the duration of the hydrothermal growth process increases [3].

Table 3: Results of N_2 adsorption isotherms

Zeolite	S_{BET} (m^2g^{-1})	$S_{Mesopore}$ (m^2g^{-1})	$S_{Langmuir}$ (m^2g^{-1})	Pore volume (cm^3g^{-1})[a]	Average pore diameter (nm)[b]
T1	88.44	81.66	137.52	0.003	5.5
T2	95.75	75.84	146.61	0.010	3.4

a. t-plot micro-pore volume
b. BJHaverageporewidth adsorption
S: Surface area

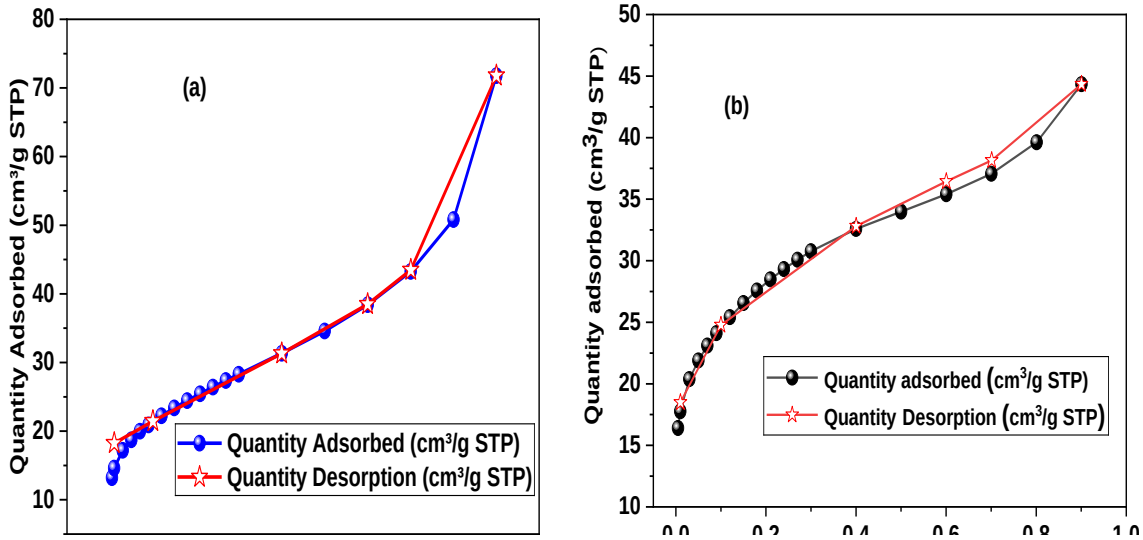

Fig. 11: N_2 adsorption -desorption isotherms of the : (a) T1 and (b) T2 zeolite

3.1.10. Thermogravimetric Analysis (TGA)

The decomposition temperature of the zeolites is an important parameter to understand the thermal stability of these products. In this section, we will focus on the TGA/DrTGA curves of the zeolites T2 and T1 are illustrated in Fig. 12 (a) and (b).

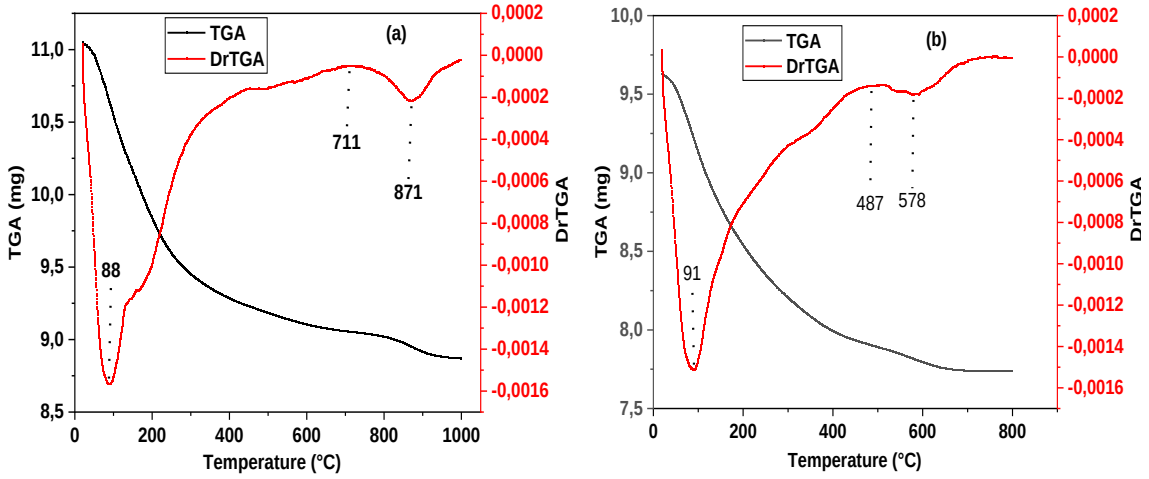

Fig. 12: DrTGA and TGAcurves of zeolites T1(A) and T2 zeolite (B).

Thermal analysis was conducted on the synthesized samples of zeolites T2 and T1. Fig. 15 displays the thermogravimetric plots. It can be inferred that when the temperature increases (30–995 °C), a slight decrease in weight is observed in zeolites T1 and T2, which can be attributed to the evaporation and dehydration of water. The weight loss percentages of the physically adsorbed water for the T1 and T2 zeolites are 19.2% and 16.4%, respectively [49]. TGA of zeolites T2 and T1 revealed a progressive reduction in mass, with an initially rapid rate of weight loss (Fig. 12).

The weights of both samples consistently decreased but at a slower rate after reaching a temperature of 450 °C. A slight inflection point was detected at approximately 518 °C for sample T2. The TGA of the zeolite T forms, T2 and T1, derived from the treated bentonite clay revealed the existence of a solitary dominant phase consisting of aluminum and silicon (Al-Si). This phase was observed at approximately 518 °C for the T2 sample [47].

The mass of zeolite T2 decreased, as observed in the TG curve, which occurred within the temperature range of 32 to 418 °C. This specific range was used to calculate the conversion factor. This stage involves the process of removing adsorbed surface water, extracting water molecules from the channels-void system of the zeolite structure, and dehydrating the hydrated cations within the zeolite framework [50]. There is a progressive weight reduction, reaching approximately 16.4%. Nevertheless, there is negligible thermal transfer within this temperature range; the weight reduction could be attributed to the evaporation of water. Between 418 and 648 °C, there is a slight weight reduction, approximately 2.1%.

This stage of weight loss is likewise linked to an exothermic reaction. Fig. 15 displays the differential thermal analysis (DTA) and TGA results for the zeolite T powders. The DTA curves for zeolites T1 and T2 exhibited wide endothermic peaks at approximately 88 and 91 °C, respectively. This signaled the elimination of water molecules that had been adsorbed. The thermal analysis revealed two exothermic peaks, T2 and T1, occurring at temperatures of 487 and 711 °C, respectively. These peaks indicate disintegration of the zeolitic lattice [51]. Two endothermic peaks were subsequently observed at temperatures of 578 and 871 °C for T2 and T1, respectively, indicating recrystallization of the material in a nonzeolitic form [52].

3.1.11. Temperature-programmed desorption (TPD)

The zeolite T2 has been found to have a peak at a lower temperature (referred to as the L peak), which is assigned to a weakly bound ammonia molecule, likely hydrogen-bonded. However, this peak does not correspond to the ammonia species that are adsorbed on the acidic site, as shown in Fig. 13.

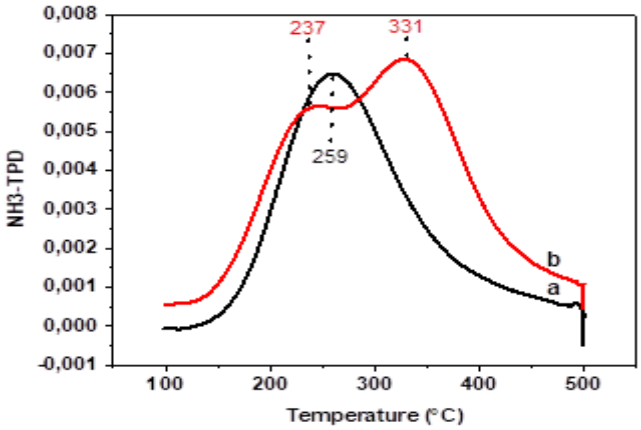

Fig. 13: NH_3-TPD profiles of zeolites T1 (a)and T2(b).

The peak observed at higher temperatures (referred to as the H peak) is attributed to the presence of a highly acidic site. The L peak does not indicate acidic properties. In contrast, the strength of the H peak indicates the existence of acid sites [53]. At high temperatures, T2 had a desorption peak that was stronger than that at low temperatures. This showed that there was not much Brønsted acid present, but there were many Lewis acid sites. The prevailing consensus in the literature is that desorption-NH_3 peaks occurring at low temperatures (100–300 °C) are typically associated with acidic sites of Brønsted, however, peaks observed at high temperatures (400–650 °C) are ascribed to acidic sites of Lewis [54]. Zeolite T1 exhibited a single peak at 256 °C (L peak), with a desorption of 0.177 mmol/g in NH_3. The absence of the H peak would be expected because the sample lacked any Lewis acid sites. The NH_3 desorption capacity for zeolite T2 was 0.277 mmol/g, and the greatest desorption occurred at 327 °C.

3.2. Characterization of BTDDB

3.2.1. The infrared spectrum

The spectrum infrared (Fig. 14**)** exposes a weak stretching band at 3385 cm^{-1} for the N-H system, four strong bands in the 3000-2850 cm^{-1} range due to the C-H stretching vibrations of asymmetric and symmetric CH and CH_3 functional groups, and at 1599 and 1493 $cm^{-1,}$ two strong bands characterize the stretching of non-localized double bonds (C=C) of the aryl groups. The strong band at 1462 cm^{-1} is due to in-plane symmetric deformation of the C-H band of the methyl group CH_3, the medium strong band at 1370 cm^{-1} is due to symmetric deformation of the methyl group CH_3, and the strong sharp band at 550 cm^{-1} results from the stretching vibration of the C-Br bond. In the deformation zone (fingerprint region), the strong band at 759 cm^{-1} is due to out-of-plane deformation of the C-H aryl system, which is consistent with what is stated in the Refs [55,56].

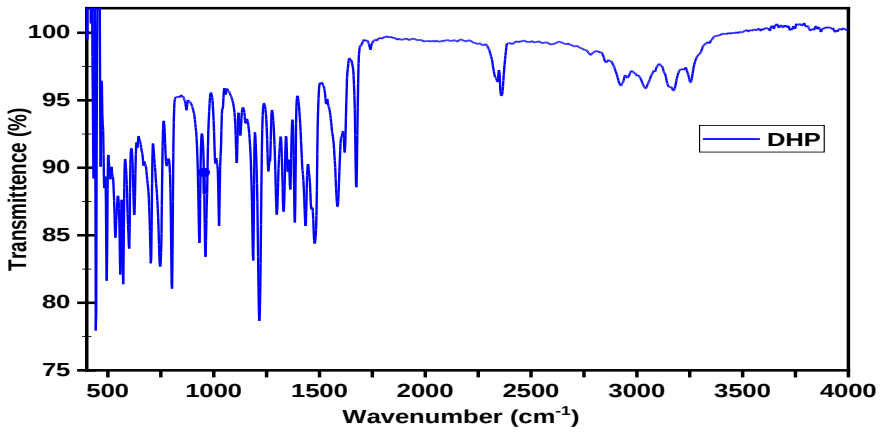

Fig. 14: FTIR study of BTDDB

3.2.2. The ^{1}H NMR spectrum

The ^{1}H NMR spectrum shows that the methyl proton groups resonated as singlets at 2.28 ppm (Fig. 15). The distinct CH group is detected as a singlet at 5.30 ppm. The protons of the aromatic system manifest as multiplets within the range of 6–7 ppm. Ultimately, the proton of the azote (NH) is observed at 7.4 ppm,which is consistent with what was mentioned in Ref [57].

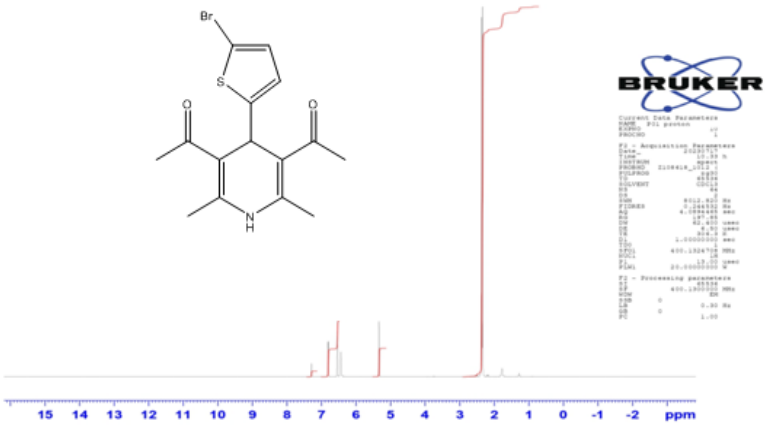

Fig 15: ^{1}H NMRstudy of BTDDB

3.2.3 ^{13}C NMR

The ^{13}C NMR spectrum (Fig. 16) shows that the carbon atoms of the methyl group are present at chemical shifts of δ 20.19 ppm and 29.97 ppm. Additionally, the carbon atom of the CH group is present at a chemical shift of δ 35.66 ppm. The carbon atoms of the Br group are observed at a chemical shift of δ 110.44 (Br-C-Ar), whereas the remaining carbon atoms of the aryl groups are observed at chemical shifts of δ 113.300, 223.94, 229.34, 144.12, and 151.84 ppm (-HC=C-) [57], and the carbon atoms of acetone are observed at δ 196.98 ppm (0=C- R). The peaks at δ 76.70, 77.02, and 77.34 ppm originate from the solvent. The chemical structure is shown in Fig. 2.

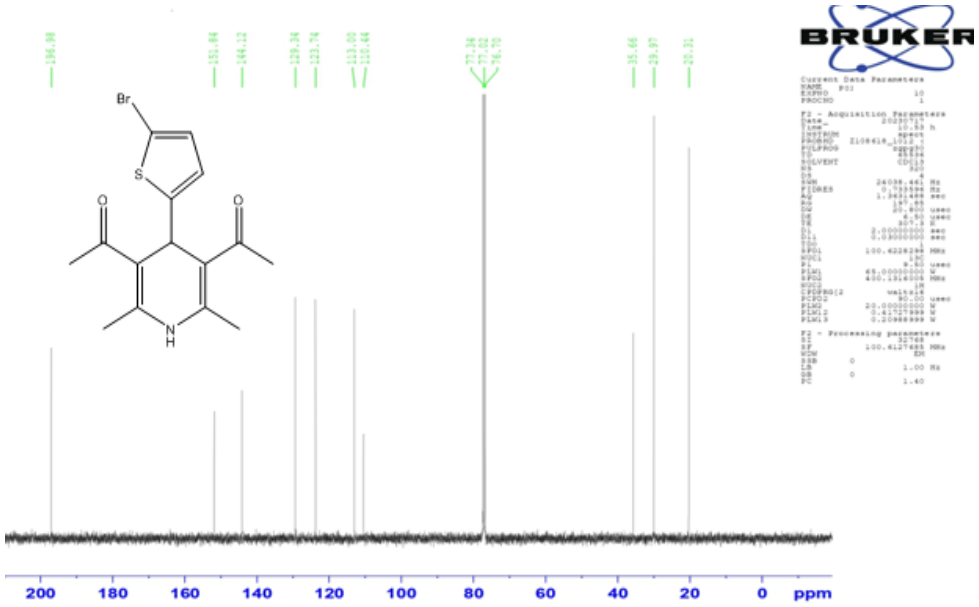

Fig. 16:NMR^{13}C study of BTDDB

3.2.4. UV study

The ultraviolet spectrum of BTDDB (Fig. 17) shows a weak signal at 270 nm, characteristic of the n → π* transition, and at 180nm and 380 nm, characteristic of the π → π* transition [58].

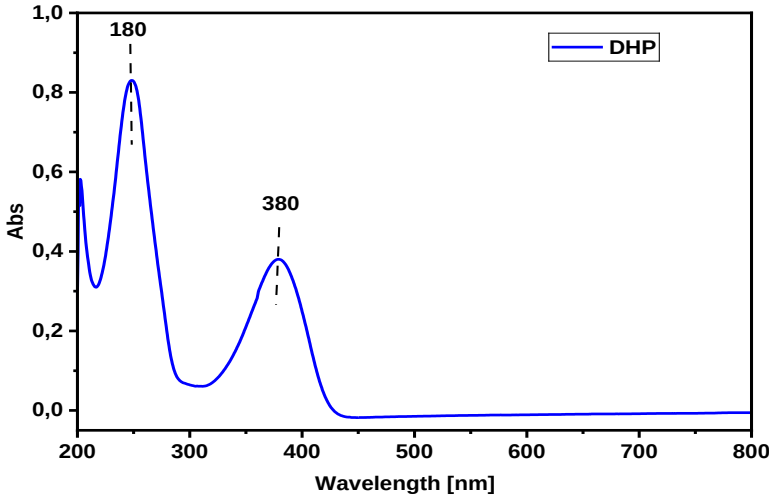

Fig. 17: UV study of BTDDB

3.3. Molecular docking

Molecular docking is a computational modeling technique used in chemistry, structural biology, and drug design. It allows predicting the interaction between a small molecule (ligand) and a target macromolecule (protein, DNA, RNA). In this section, we have presented the three-dimensional crystal structures of the receptor targets were downloaded from the Protein Data Bank with the PDB codes 4WKO and 8BN6 [59,60]. They are correctly defined structures with good resolution and are essentially determined by X-ray crystallography and NMR spectroscopy. These targets are of very interesting therapeutic interest, such as the PDB 4WKO complex,which is a gram-negative bacterial target, *Helicobacter pylori*, that is accountable for most peptic ulcers and constitutes a significant risk aspect for gastric cancer. On the other hand, the B subunit macromolecule of DNA gyrase agrees to PDB 8BN6 of the gram-positive *Staphylococcus aureus* bacterial target, which uses the rigid docking technique with MOE (Molecular Operating Environment) software [61]. This method consists of an exhaustive search in space for the optimal pose of the ligand, which is limited to positioning within the active site of the protein [62,63]. Initially, the water molecules and cocrystallized ligands were removed because of the selectivity of intermolecular interactions. The preparation and minimization of the energies of two structures (ligand and protein) were carried out by the field forces in the MMFF94x implanted in the MOE. Likewise, these structures are corrected by the addition of hydrogen [64]. The DHP ligand to be simulated is grouped in a database in mdb form, and then the docking simulation parameters are set by default. The in*silico* determination of the interaction domain of the DHP ligand on aminodeoxyfutalosine nucleosidase (PDB: 4WKO; Resolution: 1.90 Å) and Subunit B of DNA gyrase (PDB: 8BN6; Resolution: 1.60 Å) was performed. In addition, simulations of the docking of the DHP ligand in the necessary site for each target made it possible to identify the groups essential for the stabilization of this ligand. The values of the scoring energies of the ligands and their RMSDs are listed in Table 4.

Table 4. Scores of interactions associated with rigid docking of the inhibitors studied.

		S (Kcal/mol)	RMSD (Å)
4WKO	DHP[a]	-4.7203083	0.979141951
	GMD[b]	-8.86972618	1.04567194
8BN6	DHP[a]	-6.39183378	1.06948066
	R53[c]	-8.37425709	1.37301409

a. DHP: 1,1'-(4-(5-bromo-2-thiophenyl)-2,6-dimethyl-1,4-dihydropyridine-3,5-diyl)bis(ethan-1-one)
b. GMD: (3R,4S)-1-[(4-amino-5H-pyrrolo[3,2-d]pyrimidin-7-yl)methyl]-4-{[(4-hydroxybutyl) sulfanyl] methyl}pyrrolidin-3-ol

c. R53: 2-[[3,4-Bis(chloranyl)-5-methyl-1-{H}-pyrrol-2-yl]carbonylamino]-4-morpholin-4-yl-1,3-benzothiazole-6-carboxylic acid

In our investigation, the ligand–receptor complexes formed were adapted to the most stable conformation, which corresponds to the lowest energy score. On the other hand, a better assessment of the prediction of the values of the source mean square deviation (RMSD) of the designed model does not exceed 2 Å [65]. Considering these results, the DHP ligand presents a better pose docked in the binding site of each target with an affinity of -4.7203 kcal/mol and -6.3918 kcal/mol, which are score functions for the DHP-4WKO and DHP-8BN6 complexes, respectively. These complexes have very significant RMSD values compared with those of the complexes formed with the standard ligands GMD and R53. A better appreciation of the docking affinity results shown in figure 18

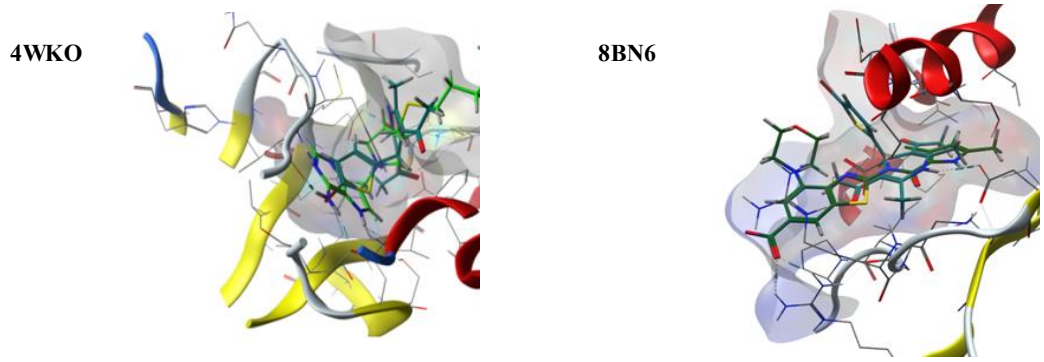

Ligands: DHP (Blue), GMD (Green) Ligands: DHP (Blue), R53 (Green)

Fig. 18: Illustration of the ligands positioned in the active site for each target

The docking results for complexes with RMSD values lower than 2Å are shown in Figure 18. The best conformation of the ligand generated (DHP) by docking (blue) is superimposed on the experimental pose of the cocrystallized ligand (colored green). In particular, to better understand the binding mechanisms involved by our ligand in the active site pocket of aminodeoxyfutalosine nucleosidase and DNA gyrase subunit B, increasing the affinity of the DHP ligand by establishing a greater number of hydrophobic interactions with respect to the aminodeoxyfutalosine nucleosidase receptor, these interactions appear with the residues Phe153, Glu173, Ala200, Val172, and Phe153, as well as hydrogen interactions with the DNA gyrase subunit B receptor (Table 5). It will therefore be very interesting to consider the mode of interaction in Fig. 19 toward the active sites of each protein target.

Table 5: Summary of the different interactions ensuring the stability of the best complexes formed with the DHP ligand.

Types of interaction	From receptor (4WKO)	To ligand (DHP)	Distances
Pi-Sulfur	MET174: Sulfur	Pi-Orbitals	4,5629
Pi-Sulfur	PHE153: Pi-Orbitals	Sulfur	4,50861
Pi-Lone Pair	PHE208: Pi-Orbitals	Lone Pair (O)	2,74712
Hydrophobic (Pi-Pi T-shaped)	PHE153: Pi-Orbitals	Pi-Orbitals	4,33914
Hydrophobic (Amide-Pi Stacked)	GLU173:C,O;MET174:N	Pi-Orbitals	5,33891
Hydrophobic (Alkyl)	ALA200: Alkyl	Alkyl	4,28445
Hydrophobic (Alkyl)	VAL172: Alkyl	Alkyl	4,48962
Hydrophobic (Pi- Alkyl)	PHE153: Pi-Orbitals	Alkyl	4,39695
Types of interaction	From receptor (8BN6)	To ligand (DHP)	Distances
Conventional Hydrogen Bond	ASP75: O	NH	2,49058
Carbon Hydrogen Bond	PRO81; H-Donor	Oxygen	2,62877
Pi-Donor Hydrogen Bond	ASN48 ; H-Donor	Pi-Orbitals	2,50785

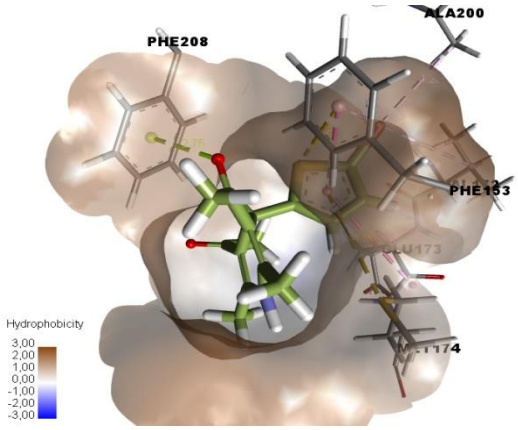

Hydrophobic interaction surface of the DHP ligand

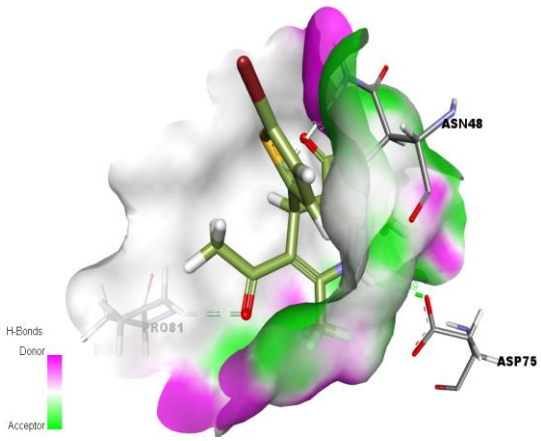

Hydrogen bond surface of DHP ligand

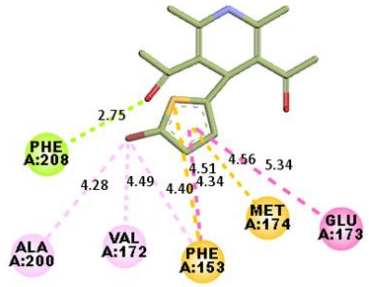

2D interaction of DHP ligand

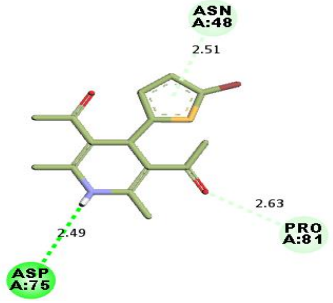

2D interaction of DHP ligand

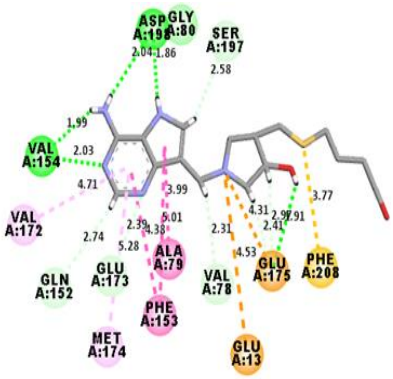

2D interaction of GMD ligand
Interaction with the 4WKO binding site

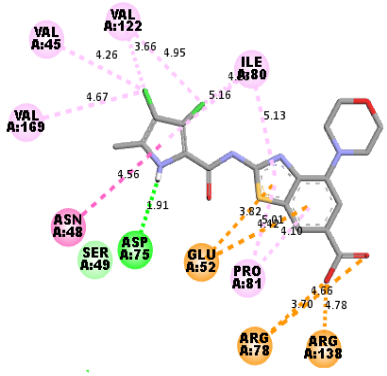

2D interaction of R53 ligand
Interaction with the 8BN6 binding site

Fig. 19: 2D and 3D interaction modes of the best poses docked in the binding sites of protein targets.

At the active site, the interaction process is carried out by electron donor and electron withdrawing groups of the ligand with the residues of the protein pocket. This association is ensured owing to several types of weak bonds. Indeed, the superimposition of the interactions of aminodeoxyfutalosine nucleosidase (DHP) and DNA gyrase subunit B (DHP) complexes with redocking of the cocrystallized ligand shows good positioning and better selectivity within the cavity of the

4WKO and 8BN6 targets, which is in good conformity with the experimental results. The bonds are hydrophobic, hydrogen and electrostatic in nature, particularly the amino acids Met174, Phe208, Phe153, Glu 173, and Val172, compared with the GMD ligand; however, the DHP ligand interacts with the amino acids Asp75, Pro81, and Asn48 compared with the R53 ligand.

3.4. Pharmacokinetic properties (ADME)

Using the server in the Refs [66,67] We were able to predict the physicochemical and pharmacokinetic properties governing the ADME criteria of the DHP ligand that inhibits both targets (Table 6).

Table 6: Physicochemical properties and ADME profile of the DHP ligand

Physico-chemical Properties						
Num. rotatable bonds	Num. H-bond acceptors	Num. H-bond donors	TPSA	Lipinski's rule	Veber's rule	Bioavailability Score
3	2	1	74.41 Å²	Yes; 0 violation	Yes; 0 violation	0.55
Profile ADME						
Absorption						
Water solubility (log mol/L)	Caco2 permeability (log Papp in 10^{-6} cm/s)	Intestinal absorption (human) (% Absorbed)	Skin Permeability (log Kp)	P-glycoprotein substrate	P-glycoprotein I inhibitor	P-glycoprotein II inhibitor
-4.463	1.399	89.299	-2.403	No	Yes	No
Distribution						
VDss (human) (log L/kg)	Fraction unbound (human) (Fu)		BBB permeability (log BB)		CNS permeability (log PS)	
0.321	0.151		0.045		-2.42	
Metabolism						
CYP2D6 substrate	CYP3A4 substrate	CYP1A2 inhibitor	CYP2C19 inhibitor	CYP2C9 inhibitor	CYP2D6 inhibitor	CYP3A4 inhibitor
No	Yes	Yes	Yes	No	No	No
Excretion						
Total Clearance (log ml/min/kg			Renal OCT2 substrate			
-0.203			No			

The Caco-2 cell monolayer is generally used as an in vitro model of the human intestinal mucosa to predict the absorption of orally directed drugs [68]. Indeed, it is important to predict the Caco-2 permeability of the DHP ligand, which was high because the higher predicted value of 0.9 for the percentage of the ligand absorbed by the human small intestine was 89.299%, which means that the absorbance of the ligand is considered elevated by the intestine.

The ligand has a solubility logS = -4.463 log mol/L, which reflects that this ligand has moderate solubility. The predicted ligand model is likely to be a nonsubstrate of P-gp. In addition, the ligand was characterized by the ability to inhibit glycoprotein I transport, which can be explained by specific therapeutic advantages [69]. The DHP ligand is of interest for the progress of transdermal drug delivery because the predicted value of relatively low skin permeability is log Kp = -2.42 > -2.5.

The steady-state distribution volume VDss of the ligand is considered low because it is less than 0.71 L/kg, and the ability of the ligand to penetrate the brain is relatively easy according to the predicted value of BBB permeability, with a positive logBB = 0.045. Penetration into the central nervous system (CNS) was found to be moderated by LogPS = -2.42 lying between -3 < Log PS < -2.

For metabolism, the ligand DHP inhibits cytochrome p450 for the isoforms CYP 1A2 and CYP 2C19, and this ligand is a substrate of the CYP3A4 isoform, which is responsible for metabolism. Furthermore, in excretion flight, total clearance is expressed as a grouping of hepatic and renal clearance and excretion by the kidney, which is linked to oral bioavailability.

The predicted drug likeness properties were acceptable and perfectly met the rules of Lipinski and Veber [70,71];therefore, the drug can be administered orally. The results revealed that the DHP ligand presented a good ADME profile and validated the Lipinski rule, thus indicating good oral bioavailability with ease of absorption or permeability in the body without causing problems. Furthermore, high oral bioavailability is frequently an important thought in the advance of bioactive molecules as therapeutics.

3.5. DFT methods

3.5.1. Density functional theory (DFT)

The computational method was applied via density functional theory (DFT) to study the electronic structure of the synthesized DHP ligand to determine the geometric structure, frontier molecular orbitals (HOMO, LUMO) and reactivity indices of this ligand, with the standard B3LYP 6-31G (d) base using Gaussian 09 software [72]. Energy minimization corresponds to the optimization of the most stable ligand geometry, and the identification of the Mulliken atomic charge distributed on the DHP ligand atoms is presented in Fig. 23.

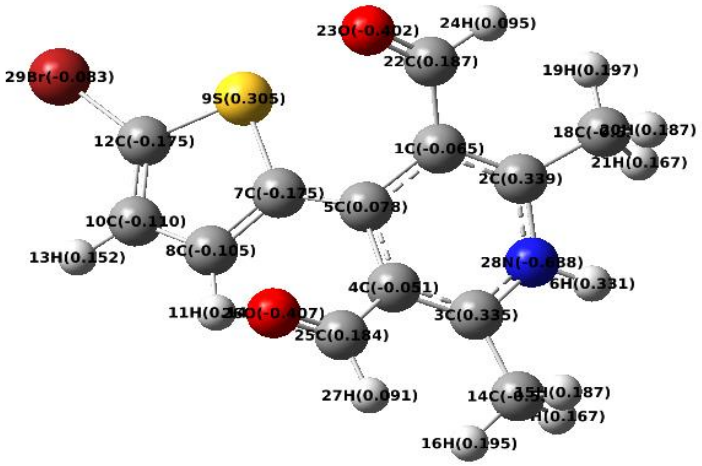

Fig 20: Optimized structure of the ligand with Mulliken atomic charge identification

Atoms that carry negative partial atomic charges of the molecular system can produce electronic orbitals to establish bonds [73].The alternating negative charges distributed on the carbon atoms, including the nitrogen atom in the pyridine ring, result in delocalization of the π electrons, leading to a mesomeric effect favoring hydrophobic interactions. Therefore, the nucleophilic attack sites are the atoms that carry negative charges, while the positive atoms probably participate in the formation of the electrophilic sites.

3.5.2. Analysis of frontier molecular orbitals and the MEP surface

The distributions of electrons in the orbital (HOMO, LUMO) and molecular electrostatic potential (MEP) of the DHP ligand are shown in Fig. 24. Molecular orbitals show a principal role in chemical reactions and the reactivity of molecules. The highest employed molecular orbital (HOMO) is associated with the ability of a molecule to donate electrons to an acceptor. On the other hand, the lowest unoccupied molecular orbital (LUMO) is associated with the capacity of a molecule to accept electrons. Notably, the higher the value of the E_{HOMO} energy of the molecule is, the greater its ability to donate electrons. Therefore, electrophilic attacks can be well correlated with atomic sites having a high density of the HOMO orbital; likewise, the higher the value of the E_{LUMO} energy is, the greater its ability to accept electrons [74]. Concerning the reactivity indices of the DHP ligand, the energy values (E_{HOMO}, E_{LUMO}) allow us to calculate the reactivity indices, which are summarized in Table 7.

ALPHA state

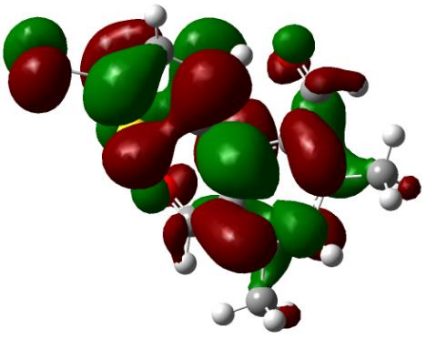

E_{GAP} = 0,07631 Ev

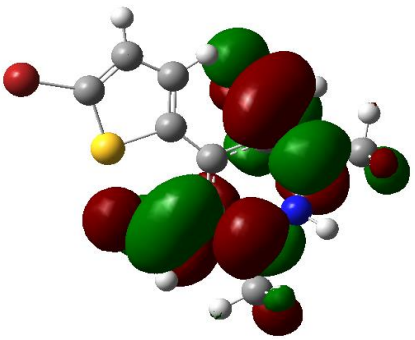

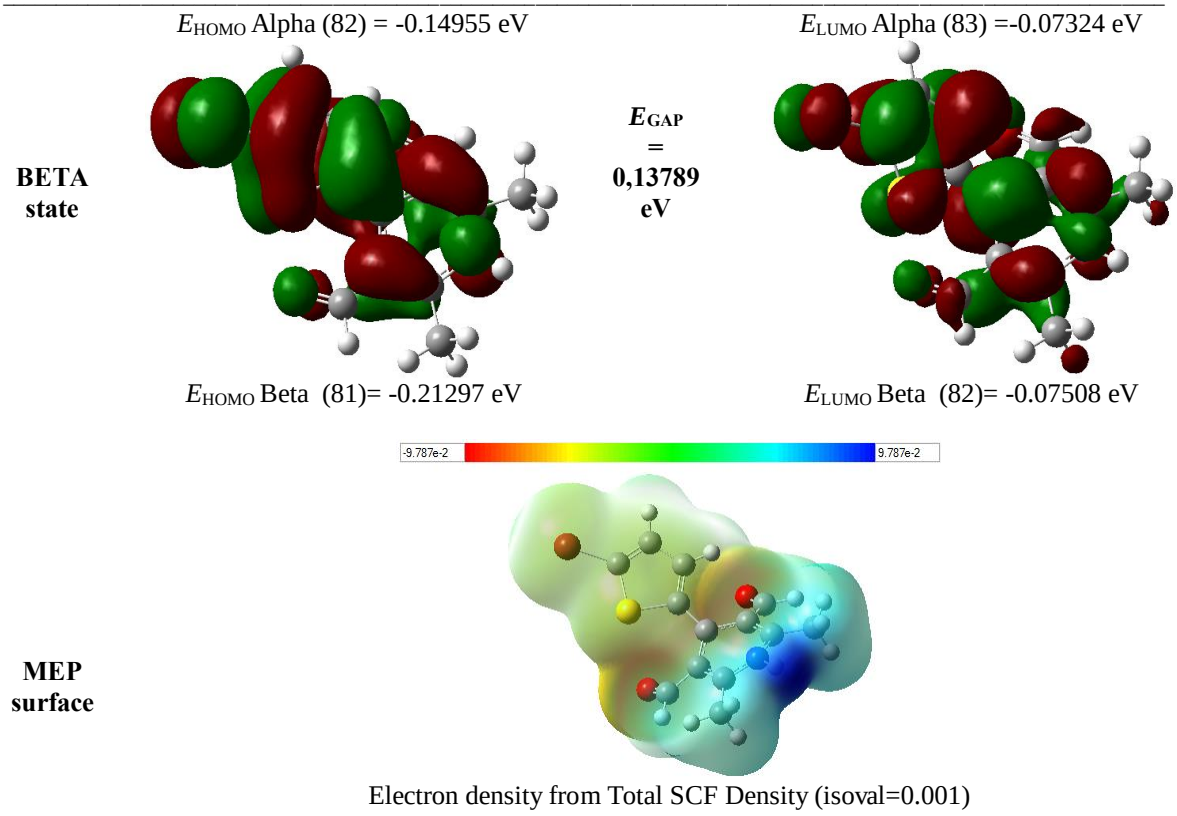

Fig. 21: Molecular orbital [HOMO (Alpha), LUMO (Beta)] and molecular electrostatic potential (MEP) surface of the DHP ligand; DFT/UB3LYP (Basis set 6-31G (d)) with spin doublet

Table 7: Calculated values of the reactivity indices of the DHP ligand in the gas phase

Electronic reactivity parameters	DHP ligand	
	Alpha state	Beta state
E_{HOMO} (eV)	-0.14955	-0.21297
E_{LUMO} (eV)	-0.07324	-0.07508
Gaps Energy (eV)	0,07631	0,13789
Total Energy (a.u)	-3677.0226	3677.0226
Ionization Potential (I) (eV)	0.14955	0.21297
Electron Affinity (A)	0.07324	0.07508
Electronegativity (χ)	0,111395	0,144025
Chemical potential (μ)	-0,111395	-0,144025
Chemical hardness (η)	0,038155	0,068945
Electrophilicity (ω)	0,16249	0,15040
Dipole moment (Debye)	10.4133	10.4133

When comparing the values of the energy gap (E_{Gap}) of the alpha and beta molecular orbitals to excite an electron from a low orbital level to a higher orbital, according to the theory of molecular orbitals, the reactivity chemical is a function of interactions between frontier molecular orbitals, i.e., the highest occupied HOMO (highest occupied molecular orbital) and the lowest vacant LUMO (lowest unoccupied molecular orbital) [75,76]. Indeed, the greater the energy gap between these orbitals is, the harder and more stable the molecule is and therefore the less reactive it is [77]. The shape of the beta orbital (E_{Gap} = 0.13789 eV) is less reactive than that of the alpha orbital (E_{Gap} = 0.07631 eV).

The application of molecular electrostatic potential (MEP) mapping is a useful indicator for determining the active centers responsible for electrophilic and nucleophilic reactions, which are associated with electron density [78]. The molecular electrostatic potential (MEP) of the DHP ligand was calculated and is presented in Figure 3. The red and yellow colors represent the negative areas of the MEP associated with electrophilic reactivity, whereas the blue color represents the positive

areas related to the reactivity of the nucleophile. Notably, the DHP ligand, which contains the negative site, is located at the level of the O carbonyl group, while the positive regions possible for nucleophilic attack are around the hydrogen atoms.

4. Conclusion

This study successfully synthesized zeolite T aggregates with spherical crystals resembling Saharan flowers. This was achieved by using the hydrothermal method with different durations of crystallization with bentonite treated as an aluminum source. An inclusive investigation was conducted on the crystallization process of zeolite T. The optimum treatment temperature for producing zeolite T2, which has a molar composition of $1Al_2O_3$, 25 SiO_2, $6.5Na_2O$, $2.25K_2O$, and 350 H_2O as the dominant phase in the system, was determined via analytical techniques such as FTIR, RAMAN, DRX, SEM, EDS, TPD, ATG, and N_2 adsorption–desorption (BET). The analysis revealed that an optimal treatment temperature is 130 °C for 5 days. Nucleation of zeolite T from treated bentonite began after 3 days. The results indicate that zeolite T2, composed of uniform nanocrystalline grains produced over 5 days, forms a mesoporous zeolite T with a size of 1.35 µm and a molar ratio of 1.78. An analysis of the BET (surface area) revealed a value of 95.75 m^2g^{-1}, accompanied by a pore volume of 0.010 cm^3g^{-1}. Moreover, TPD-NH_3analysis revealed limited Brønsted acid sites but a significant number of Lewis acid sites. Due to their unique morphology and microporosity, zeolite T2 aggregates show promise for industrial applications, including catalysis, adsorption, and separation. The application of zeolite T2 as a catalytic agent in the Hantzsch reaction was effective in the synthesis of BTDDB , achieving a yield of 70%. FTIR, NMR, UV spectroscopy, and mass spectrometry confirmed that the crystalline product was indeed BTDDB. The molecular docking method and computational method were applied via density functional theory (DFT) to BTDDB. During this work, we considered a computational study involving molecular docking to evaluate the inhibition of the targets aminodeoxyfutalosine nucleosidase (PDB: 4WKO) and DNA gyrase subunit B (PDB: 8BN6), making it possible to highlight the main interactions that guide and orient the best conformers of DHP within these targets, which are of the hydrophobic or hydrogen type. The results revealed the possibility of retaining the DHP ligand to obtain a new structure for therapeutic use**.** These materials (zeolite T2) offer large advantages in terms of recyclability, energy efficiency, and waste reduction, aligning the practice of chemistry with the principles of green chemistry. Continued research in this area is essential to overcome the remaining challenges and fully exploit the potential of these materials for future applications.

5. References

[1] G.A. Ozin, A. Kuperman, A. Stein, Advanced zeolite, materials science, Angew. Chemie Int. Ed. English. 28 (1989) 359–376.https://doi.org/10.1002/anie.198903591

[2] S. Van Donk, A.H. Janssen, J.H. Bitter, K.P. de Jong, Generation, characterization, and impact of mesopores in zeolite catalysts, Catal. Rev. 45 (2003) 297–319.https://doi.org/10.1081/CR-120023908

[3] N. Jusoh, Y.F. Yeong, M. Mohamad, K.K. Lau, A.M. Shariff, Rapid-synthesis of zeolite T via sonochemical-assisted hydrothermal growth method, Ultrason. Sonochem. 34 (2017) 273–280.https://doi.org/10.1016/j.ultsonch.2016.05.033

[4] M. Mirfendereski, T. Mohammadi, Investigation of hydrothermal synthesis parameters on characteristics of T type zeolite crystal structure, Powder Technol. 206 (2011) 345–352.https://doi.org/10.1016/j.powtec.2010.10.003

[5] S.E. Arshad, M.L. Rahman, S.M. Sarkar, E.F. Yusslee, S.Z. Patuwan, Hydrothermal synthesis of zeolite T from kaolin using two different structure-directing agents, Mater. Res. Express. 5 (2018) 15011.DOI 10.1088/2053-1591/aa9d05

[6] S. Zaiou, O. Beldjebli, D. Belfennache, M. Tayeb, F. Zenikheri, A. Harabi, Effect of CaF_2 addition on the densification behavior and mechanical properties of resistant anorthite and its bioactivity., Dig. J. Nanomater. Biostructures. 18(1) (2023) 69-82.DOI: 10.15251/DJNB.2023.181.69

[7] R. Ouldamer, D. Madi, D. Belfennache, Hydrogen Diffusion Study via Phosphorus Deactivation in n-Type SiliconIn: Hatti, M. (eds) Advanced Computational Techniques for Renewable Energy Systems. IC-AIRES 2022. Lecture Notes in Networks and Systems, Springer,591 (2023) 700-705.https://doi.org/10.1007/978-3-031-21216-1_71

[8] Y. Benkrima, D. Belfennache, R. Yekhlef, A.M. Ghaleb, First-principle investigations of structural and optical properties of CdSe., Chalcogenide Lett. 20 (2023) 609-618.https://doi.org/10.15251/CL.2023.208.609

[9] M.R. Asrori, A. Santoso, S. Sumari, Proofing the presence of metal oxide impregnated into zeolite A without calcination: XRD and FTIR studies, Case Stud. Chem. Environ. Eng. 9 (2024) 100676. https://doi.org/10.1016/j.cscee.2024.100676.

[10] D. Belfennache, N. Brihi, D. Madi,Effective phosphorus deactivation in schottky diodes hydrogenated in MW-ECR plasma reactor Proceeding of the IEEE xplore, 8th (ICMIC) (2016). 7804164. 497–502 (2017). https://doi.org/10.1109/ICMIC.2016.7804164

[11] S. Mahdid, D. Belfennache, D. Madi, M. Samah, R. Yekhlef, Y. Benkrima, Defects passivation and H-diffusion controlled by emitter region in polysilicon solar cells submitted to hydrogen plasma., J. Ovonic Res. 19(5) (2023)535-545.https://doi.org/10.15251/JOR.2023.195.535

[12] Y. Li, G. Li, H. Li, W. Liu, J. Ji, S. Lu, Z. Li, H. Peng, Promoting metal oxides–zeolite electron interaction on MnCeOx/HY catalyst for boosting nitrogen oxides reduction, Appl. Catal. B Environ. Energy. 360 (2025)

124535.https://doi.org/10.1016/j.apcatb.2024.124535
[13] H. Liu, X. Zhou, K. Xu, H. Zhang, H. Wang, H. Zhou, H. Chen, Mesoporous TS-1 zeolite-confined metal oxides photocathode for efficient reduction of carbon dioxide to methanol, Chem. Eng. J. 489 (2024) 151483.https://doi.org/10.1016/j.cej.2024.151483.
[14] X. Yin, N. Liu, M. Han, F. Xu, Y. Jia, F. Song, H. Cui, Ultrasonic-pretreated hydrothermal synthesis of less dense zeolite CHA from the transformation of zeolite T, Ultrason. Sonochem., 100 (2023) 106598, https://doi.org/10.1016/j.ultsonch.2023.106598.
[15] J. Liu, J. Zhang, H. Zhang, F. Zhang, M. Zhu, N. Hu, X. Chen, H. Kita, Synthesis of hierarchical zeolite nanocrystals with the assistance of zeolite seed solution,J. Solid State Chem.285 (2020)121228https://doi.org/10.1016/j.jssc.2020.121228.
[16] X. Yin, N. Chu, X. Lu, Z. Li, H. Guo, Studies on the formation of hierarchical zeolite T aggregates with well-defined morphology in different template systems, Solid State Sci. 51 (2016) 30–39.https://doi.org/10.1016/j.solidstatesciences.2015.11.007
[17] S.E. Arshad, E.F. Yusslee, M.L. Rahman, S.M. Sarkar, S.Z. Patuwan, Hydrothermal synthesis of free-template zeolite T from kaolin, in: AIP Conf. Proc., AIP Publishing, 1901(1), (2017).https://doi.org/10.1063/1.5010469.
[18]M. V. Rodrigues, P. Vinaches, C. C. Polo, M. M. Silva, A. F. Suzana, W. Cha, S. B. Pergher, A. Rochet, F. Meneau, In situ visualisation of zeolite anisotropic framework flexibility during catalysis,Catalysis Today, 446 (2025)115118, https://doi.org/10.1016/j.cattod.2024.115118.
[19] J. Tan, Y. Xiao, G. Liu, W. Chen, A. Zheng, Mechanism of confinement compensating for acid strength: The case of aromatic Wheland intermediate formation in zeolite catalysis, Micropor. Mesopor. Mat., 387 (2025) 113515, https://doi.org/10.1016/j.micromeso.2025.113515.
[20]S. Bohra, K.P. Dey, D. Kundu, M.K. Naskar, Synthesis of zeolite T powders by direct dissolution of rice husk ash: an agro-waste material, J. Mater. Sci. 48 (2013) 7893–7901.https://doi.org/10.1007/s10853-013-7499-y
[21] L. Yan, S. Chen, P. Wang, X. Liu, L. Han, T. Yan, Y. Li, D. Zhang, Hydrothermally stable metal oxide-zeolite composite catalysts for low-temperature NOx reduction with improved N_2 selectivity, Chinese Chem. Lett. 35 (2024) 109132.https://doi.org/10.1016/j.cclet.2023.109132.
[22] L.H.R. Alponti, M. Picinini, E.A. Urquieta-Gonzalez, A.G. Correa, USY-zeolite catalyzed synthesis of 1, 4-dihydropyridines under microwave irradiation: Structure and recycling of the catalyst, J. Mol. Struct. 1227 (2021) 129430.https://doi.org/10.1016/j.molstruc.2020.129430
[23] I. F Nassar, W.A El-Sayed, T.I. M. Ragab, A.S. G. Shalaby, A Mehany Design, synthesis of New Pyridine and Pyrimidine Sugar Compounds as Antagonists targeting the ERα via structure-based virtual screening, Mini Reviews in Medicinal Chemistry, 19(5) , (2019) 395-409.DOI: 10.2174/1389557518666180820125210
[24] E. Mansour, A.A .Abd-Rabou, I.F Nassar, S.I Elewa, Synthesis, Docking and Anticancer Evaluation of New Pyridine-3-Carbonitrile Derivatives, Polycycl. Aromat. Compd.42 (6) (2022) 3523–3544. DOI: 10.1080/10406638.2020.1870507
[25] MG Abouelenein, AA El-Rashedy, HM Awad, AF El Farargy, I.F Nassar, Synthesis, molecular modeling Insights, and anticancer assessment of novel polyfunctionalized Pyridine congeners, Bioorganic Chemistry. 141(2023) 106910 DOI:10.1016/j.bioorg.2023.106910.
[26] C. McLaughlin, J. Bitai, L. J. Barber, A. M. Z. Slawin, A. D. Smith, Catalytic enantioselective synthesis of 1,4-dihydropyridines via the addition of C(1)-ammonium enolates to pyridinium salts††Electronic supplementary information (ESI) available: Full characterisation and HPLC spectra. CCDC 2091719. For ESI and crystallographic data in CIF or other electronic format see, Chemical Science, 12(36) (2021) 12001-12011, https://doi.org/10.1039/d1sc03860e.
[27] T. Q. Hung, B. V. Phuc, P. T. T. Loan, D. T. L. Nhi, H. Nguyen, H. X. Vu, D. Van, T. T. Dang,,Practical Synthesis of 1,4-Dihydropyridines on Heterogeneous Sulfonic-modified Silica (SBA-15-SO_3H) Catalyst Under Mild Condition,Curr. Org. Synth., 20(8) (2023) 880-889, https://doi.org/10.2174/1570179420666230301143027.
[28] U. Kusampally, N. Dhachapally, R. Kola, C.R. Kamatala, Zeolite anchored Zr-ZSM-5 as an eco-friendly, green, and reusable catalyst in Hantzsch synthesis of dihydropyridine derivatives, Mater. Chem. Phys. 242 (2020) 122497.https://doi.org/10.1016/j.matchemphys.2019.122497
[29] K. Abdmeziem-Hamoudi, B. Siffert, Synthesis of molecular sieve zeolites from a smectite-type clay material, Appl. Clay Sci. 4 (1989) 1–9.https://doi.org/10.1016/0169-1317(89)90010-0
[30] A.K. Kushwaha, N. Gupta, M.C. Chattopadhyaya, Removal of cationic methylene blue and malachite green dyes from aqueous solution by waste materials of Daucus carota, J. Saudi Chem. Soc. 18 (2014) 200–207. https://doi.org/10.1016/j.jscs.2011.06.011.
[31] F. Belalia, A. Harichanea, D. Belfennache, R.Yekhlef, S. Zaiou, Mohamed Hemdan, M. A. Ali, Elimination of Inorganic Pollutants Using a Novel Biomaterial Adsorbent, Egypt. J. Chem. 67(13) (2024) 1167-1176. https://doi.org/10.21608/ejchem.2024.280399.9541.
[32] L. Vaculíková, E. Plevová, M. Ritz, Characterization of montmorillonites by infrared and raman spectroscopy for preparation of polymer-clay nanocomposites, J. Nanosci. Nanotechnol. 19 (2019) 2775–2781.https://doi.org/10.1166/jnn.2019.15877
[33] K. Bahranowski, A. Klimek, A. Gaweł, E.M. Serwicka, Rehydration driven Na-activation of bentonite—Evolution of the clay structure and composition, Materials (Basel). 14 (2021) 7622.https://doi.org/10.3390/ma14247622
[34] G.N. Vayssilov, H.A. Aleksandrov, E. Dib, I.M. Costa, N. Nesterenko, S. Mintova, Superacidity and spectral

signatures of hydroxyl groups in zeolites, Microporous Mesoporous Mater. 343 (2022) 112144.https://doi.org/10.1016/j.micromeso.2022.112144

[35] E.M. Flanigen, L.B. Sand, Molecular sieve zeolites-I, ACS Publications,1 (1974) 201-229.DOI: 10.1021/ba-1971-0101.ch016

[36] H. Mahadevan, K. Anoop Krishnan, R.R. Pillai, S. Sudhakaran, Stirring-ageing technique to develop zirconium-pillared bentonite clay along with its surface profiling using various spectroscopic techniques, Res. Chem. Intermed. 46 (2020) 639–660.https://doi.org/10.1007/s11164-019-03982-2

[37] D. Dumlu, S. Karadeniz, T. K. Kanatlı, E. Ceylan, M. Bayrakdar, N. Ayas, Synthesis of bentonite-supported Ni, La, and Ca catalysts for hydrogen production through steam reforming of acetic acid,Int. J. Hydrogen Energy, 85(2024), 976-996, https://doi.org/10.1016/j.ijhydene.2024.08.299.

[38] F. Pechar, D. Rykl, Study of the complex vibrational spectra of natural zeolite chabazite, Zeolites. 3 (1983) 333–336.https://doi.org/10.1016/0144-2449(83)90178-1

[39] P.M. Kester, J.T. Crum, S. Li, W.F. Schneider, R. Gounder, Effects of Brønsted acid site proximity in chabazite zeolites on OH infrared spectra and protolytic propane cracking kinetics, J. Catal. 395 (2021) 210–226.https://doi.org/10.1016/j.jcat.2020.12.038

[40] Y. Zhang, H. Han, X. Wang, M. Zhang, Y. Chen, C. Zhai, H. Song, J. Deng, J. Sun, C. Zhang, Utilization of NaP zeolite synthesized with different silicon species and $NaAlO_2$ from coal fly ash for the adsorption of Rhodamine B, J. Hazard. Mater. 415 (2021) 125627.https://doi.org/10.1016/j.jhazmat.2021.125627.

[41] Y. Yu, G. Xiong, C. Li, F.-S. Xiao, Characterization of aluminosilicate zeolites by UV Raman spectroscopy, Microporous Mesoporous Mater. 46 (2001) 23–34.https://doi.org/10.1016/S1387-1811(01)00271-2.

[42] F. Ayari, E. Srasra, M. Trabelsi-Ayadi, Characterization of bentonitic clays and their use as adsorbent, Desalination. 185 (2005) 391–397.https://doi.org/10.1016/j.desal.2005.04.046

[43] F. Hadji, Y. Rassim, D. Belfennache, R. Yekhlef, N. Bounar, M. Amokrane Bradai, M. Hemdan, M. A Ali, Non-Isothermal Kinetics of Coats-Red Fern in the Critical Points: Formation of $Al_{2-x}Cr_xO_3$ (x= 0.02) powders obtained by Sol-Gel Method, Egypt. J. Chem. 68 (2025) 63–78.https://doi.org/10.21608/ejchem.2024.283147.9600

[44] T. Battiston, D. Comboni, F. Pagliaro, P. Lotti, M. Hanfland, K. Glazyrin, H-P. Liermann, G. D. Gatta, Pressure-mediated crystal-fluid interaction in the zeolite offretite, J. Solid State Chem., 320 (2023) 123847. https://doi.org/10.1016/j.jssc.2023.123847.

[45] T. Battiston, D. Comboni, F. Pagliaro, P. Lotti, M. Hanfland, G. D. Gatta, High-pressure behavior and crystal-fluidinteraction in natural erionite-K, Mater. Chem. Phys.292 (2022)126760, https://doi.org/10.1016/j.matchemphys.2022.126760.

[46] R. Zhou, L. Hu, Y. Zhang, N. Hu, X. Chen, X. Lin, H. Kita, Synthesis of oriented zeolite T membranes from clear solutions and their pervaporation properties, Microporous Mesoporous Mater. 174 (2013) 81–89.https://doi.org/10.1016/j.micromeso.2013.02.019

[47] T. A. Chinar, M. Benbouzid, Preparation and characterization of an efficient zeolitic material from a local natural kaolinitic clay and its uses in the elimination of an organic dye, Eur. J. Chem. 7 (4) (2016) 410-415. https://doi.org/10.5155/eurjchem.7.4.410-415.1486

[48] K.S.W. Sing, Reporting physisorption data for gas/solid systems with special reference to the determination of surface area and porosity (Recommendations 1984), Pure Appl. Chem. 57 (1985) 603–619.https://doi.org/10.1351/pac198557040603

[49] N.S. Ahmedzeki, S. Yilmaz, B.A. Al-Tabbakh, Synthesis and characterization of nanocrystalline zeolite Y, Al-Khwarizmi Eng. J. 12 (2016) 79–89.https://www.iasj.net/iasj/download/a48f85277a72c412

[50] I. Majchrzak-Kucęba, A simple thermogravimetric method for the evaluation of the degree of fly ash conversion into zeolite material, J. Porous Mater. 20 (2013) 407–415.https://doi.org/10.1007/s10934-012-9610-1

[51] N.M. Musyoka, L.F. Petrik, E. Hums, A. Kuhnt, W. Schwieger, Thermal stability studies of zeolites A and X synthesized from South African coal fly ash, Res. Chem. Intermed. 41 (2015) 575–582.DOI https://doi.org/10.1007/s11164-013-1211-3

[52] S. Akbar, T.H. Shah, R. Shahnaz, G. Sarwar, Thermal studies of synthetic NaX zeolite and its zinc exchanged forms, Jour. Chem. Soc. Pak. 29 (2007). https://jcsp.org.pk/ArticleUpload/1137-5023-1-RV.pdf

[53] N. Katada, H. Igi, J.-H. Kim, M. Niwa, Determination of the acidic properties of zeolite by theoretical analysis of temperature-programmed desorption of ammonia based on adsorption equilibrium, J. Phys. Chem. B. 101 (1997) 5969–5977.https://doi.org/10.1021/jp9639152

[54] Y. Hou, Y. Li, Q. Li, Y. Liu, Z. Huang, Insight into the role of TiO_2 modified activated carbon fibers for the enhanced performance in low-temperature NH3-SCR, Fuel. 245 (2019) 554–562. https://doi.org/10.1016/j.fuel.2019.02.046.

[55] D. Febriantini, C. Herry, R.T. Yunarti, A. R. Liandi, B. Ardiansah, Microwave-assisted one-pot multicomponent synthesis of 1,4-dihydropyridine derivatives using nanochitosan, AIP Conference Proceedings 2168(1) (2019) 020068. DOI: 10.1063/1.5132495

[56] L. Moradi, M.Zare,Ultrasound-promoted green synthesis of 1,4-dihydropyridines using fuctionalized MWCNTs as a highly efficient heterogeneous catalyst, Green Chem. Lett. Rev., 11(3) (2018) 197–208. https://doi.org/10.1080/17518253.2018.1458160

[57] M. Petrova, R. Muhamadejev, B. Vigante, G. Duburs, E. Liepinsh, Intramolecular hydrogen bonds in 1,4-

dihydropyridine derivatives,R Soc Open Sci. 5(6) (2018) 180088. doi: 10.1098/rsos.180088.
[58] Y.A. Mikheev, Y.A. Ershov, Assignment of the π → π* and n → π* Transitions to the Spectral Bands of Azobenzene and Dimethylaminoazobenzene. Russ. J. Phys. Chem. 92 (2018) 1499–1507. https://doi.org/10.1134/S0036024418080174
[59] S. Wang, S.A. Cameron, K. Clinch, G.B. Evans, Z. Wu, V.L. Schramm, P.C. Tyler, New antibiotic candidates against Helicobacter pylori, J. Am. Chem. Soc. 137 (2015) 14275–14280.https://doi.org/10.1021/jacs.5b06110.
[60] M. Durcik, A.E. Cotman, Z. Toplak, S. Mozina, Z. Skok, P.E. Szili, M. Czikkely, E. Maharramov, T.H. Vu, M.V. Piras, New dual inhibitors of bacterial topoisomerases with broad-spectrum antibacterial activity and in vivo efficacy against vancomycin-intermediate Staphylococcus aureus, J. Med. Chem. 66 (2023) 3968–3994.https://doi.org/10.1021/acs.jmedchem.2c01905
[61] M. Lahyaoui, H. El-Idrissi, T. Saffaj, B. Ihssane, N. Saffaj, R. Mamouni, Y.K. Rodi, QSAR modeling, molecular docking and molecular dynamic simulation of phosphorus-substituted quinoline derivatives as topoisomerase I inhibitors, Arab. J. Chem. 16 (2023) 104783.https://doi.org/10.1016/j.arabjc.2023.104783
[62] H. Gohlke, G. Klebe, Approaches to the description and prediction of the binding affinity of small-molecule ligands to macromolecular receptors, Angew. Chemie Int. Ed. 41 (2002) 2644–2676.https://doi.org/10.1002/1521-3773(20020802)41:15<2644::AID-ANIE2644>3.0.CO;2-O
[63] G.M. Morris, M. Lim-Wilby, Molecular docking, Mol. Model. Proteins. (2008) 365–382.https://doi.org/10.1007/978-1-59745-177-2_19
[64] S. Vilar, G. Cozza, S. Moro, Medicinal Chemistry and the Molecular Operating Environment (MOE): Application of QSAR and Molecular Docking to Drug Discovery, Curr. Top. Med. Chem. 8 (2008) 1555–1572. https://doi.org/10.2174/156802608786786624.
[65] U. Roy, L.A. Luck, Molecular modeling of estrogen receptor using molecular operating environment, Biochem. Mol. Biol. Educ. 35 (2007) 238–243.https://doi.org/10.1002/bmb.65
[66] D. Ranjith, C. Ravikumar, SwissADME predictions of pharmacokinetics and drug-likeness properties of small molecules present in Ipomoea mauritiana Jacq, J. Pharmacogn. Phytochem. 8 (2019) 2063–2073.https://www.phytojournal.com/archives/2019/vol8issue5/PartAL/8-5-415-571.pdf
[67] D.E. V Pires, T.L. Blundell, D.B. Ascher, pkCSM: predicting small-molecule pharmacokinetic and toxicity properties using graph-based signatures, J. Med. Chem. 58 (2015) 4066–4072.https://doi.org/10.1021/acs.jmedchem.5b00104.
[68] W.J. Egan, K.M. Merz, J.J. Baldwin, Prediction of drug absorption using multivariate statistics, J. Med. Chem. 43 (2000) 3867–3877.https://doi.org/10.1021/jm000292e
[69] A. Daina, O. Michielin, V. Zoete, SwissADME: a free web tool to evaluate pharmacokinetics, drug-likeness and medicinal chemistry friendliness of small molecules, Sci. Rep. 7 (2017) 42717.https://doi.org/10.1038/srep42717
[70] C.A. Lipinski, F. Lombardo, B.W. Dominy, P.J. Feeney, Experimental and computational approaches to estimate solubility and permeability in drug discovery and development settings, Adv. Drug Deliv. Rev. 23 (1997) 3–25.https://doi.org/10.1016/S0169-409X(96)00423-1
[71] D.F. Veber, S.R. Johnson, H.-Y. Cheng, B.R. Smith, K.W. Ward, K.D. Kopple, Molecular properties that influence the oral bioavailability of drug candidates, J. Med. Chem. 45 (2002) 2615–2623.https://doi.org/10.1021/jm020017n
[72] M. Caricato, M.J. Frisch, J. Hiscocks, M.J. Frisch, Gaussian 09: IOps Reference, Gaussian Wallingford, CT, USA, (2009).ISBN: 978-1-935522-02-7
[73] V. Asati, S.S. Thakur, N. Upmanyu, S.K. Bharti, Virtual screening, molecular docking, and DFT studies of some thiazolidine-2, 4-diones as potential PIM-1 kinase inhibitors, ChemistrySelect. 3 (2018) 127–135.https://doi.org/10.1002/slct.201702392
[74] M.J.S. Dewar, A critique of frontier orbital theory, J. Mol. Struct. THEOCHEM. 200 (1989) 301–323.https://doi.org/10.1016/0166-1280(89)85062-6
[75] A. González, J. Casado, M.G. Gündüz, B. Santos, A. Velázquez-Campoy, C. Sarasa-Buisan, M.F. Fillat, M. Montes, E. Piazuelo, Á. Lanas, 1, 4-Dihydropyridine as a promising scaffold for novel antimicrobials against Helicobacter pylori, Front. Microbiol. 13 (2022) 874709.doi: 10.3389/fmicb.2022.874709
[76] B.S. Kulkarni, A. Tanwar, S. Pal, Reactivity descriptors and electron density analysis for ligand chemistry: A case study of 2, 2′-bipyridine and its analogues, J. Chem. Sci. 119 (2007) 489–499. https://doi.org/10.1007/s12039-007-0062-0
[77] N. Flores-Holguín, J. Frau, D. Glossman-Mitnik, Calculation of the Global and Local Conceptual DFT Indices for the Prediction of the Chemical Reactivity Properties of Papuamides A–F Marine Drugs, Molecules. 24 (2019) 3312.https://doi.org/10.3390/molecules24183312
[78] M.E. Elshakre, M.A. Noamaan, H. Moustafa, H. Butt, Density functional theory, chemical reactivity, pharmacological potential and molecular docking of dihydrothiouracil-indenopyridopyrimidines with human-DNA topoisomerase II, Int. J. Mol. Sci. 21 (2020) 1253.https://doi.org/10.3390/ijms21041253